

21

ABSTRACT

22 Arctic sea ice has declined rapidly over the past four decades and climate models
23 project a seasonally ice-free Arctic Ocean by the middle of this century, with attendant
24 consequences for regional climate. However, modeling studies lack consensus on how the
25 large-scale atmospheric circulation will respond to Arctic sea ice loss. In this study, the
26 authors conduct a series of 200-member ensemble experiments with the Community
27 Atmosphere Model version 6 (CAM6) to isolate the atmospheric response to past and
28 future sea ice loss following the Polar-Amplification Model Inter-comparison Project
29 (PAMIP) protocol. They find that the stratospheric polar vortex response is small compared
30 to internal variability, which in turn influences the signal-to-noise of the wintertime
31 tropospheric circulation response to ice loss. In particular, a strong (weak) stratospheric
32 polar vortex induces a positive (negative) tropospheric Northern Annular Mode (and North
33 Atlantic Oscillation), obscuring the forced component of the tropospheric response, even
34 in 100-member averages. Stratospheric internal variability is closely tied to upward wave
35 propagation from the troposphere and can be explained by linear wave interference
36 between the anomalous and climatological planetary waves. Implications for the detection
37 of recent observed trends and model realism are also presented. These results highlight the
38 inherent uncertainty of the large-scale tropospheric circulation response to Arctic sea ice
39 loss arising from stratospheric internal variability.

40 **1. Introduction**

41 Arctic sea ice has declined rapidly over the past four decades (Fetterer et al. 2017) and
42 the vast majority of climate models participating in the Coupled Model Intercomparison
43 Project Phase 6 (CMIP6) project a seasonally ice-free Arctic Ocean by 2050 in all emission
44 scenarios (Notz and SIMIP community 2020). The loss of sea ice and its consequences for
45 the global climate system are one of the grand science challenges of the World Climate
46 Research Programme (WCRP). Sea ice loss causes near-surface warming and increased
47 precipitation at high latitudes, especially in winter (e.g., Screen and Simmonds 2010; Deser
48 et al. 2010) due to enhanced upward fluxes of heat and moisture from the ocean to the
49 atmosphere. The remote response, however, is more complex in its physical mechanisms,
50 and there is less consensus among different studies (e.g., Cohen et al. 2020). In particular,
51 whether observed Arctic sea ice loss has contributed to colder winters over North America
52 and Eurasia in recent decades remains a topic of extensive debate (Overland et al. 2011;
53 Cohen et al. 2013; Mori et al. 2014; Perlwitz et al. 2014; McCusker et al. 2016; Sun et al.
54 2016; Ogawa et al. 2018; Blackport et al. 2019; Dai and Song 2020), highlighting the
55 challenge of distinguishing the sea ice loss effect from internal variability and the
56 incomplete mechanistic understanding of the underlying processes (Barnes and Screen
57 2015).

58 Previous modeling studies have revealed aspects of the dynamical mechanisms
59 connecting Arctic sea ice loss to large-scale atmospheric circulation changes. For example,
60 Deser et al. (2004) suggested there is a direct and an indirect component of the winter
61 atmospheric circulation response to Arctic sea ice loss. The direct component is localized
62 to the vicinity of the ice loss region and exhibits a baroclinic structure in the vertical with

63 a surface trough and upper-level ridge. The indirect component is hemisphere in scale and
64 barotropic in the vertical throughout the troposphere resembling the Northern Annular
65 Mode (NAM; Thompson and Wallace 2000) or North Atlantic Oscillation (NAO; Hurrell
66 1995). More recently, it has been argued that Arctic sea ice loss can also cause a weakening
67 of the stratospheric polar vortex, which subsequently induces a negative phase of the
68 tropospheric NAM/NAO in late winter (Peings and Magnusdottir 2014; Kim et al. 2014;
69 Sun et al. 2015). This “stratospheric pathway” is distinct from the “tropospheric pathway”
70 (i.e., that presented in Deser et al. 2004), and has been suggested to play a dominant role
71 in the inferred atmospheric circulation response to observed sea ice loss in the Barents-
72 Kara Seas (Jaiser et al. 2013; Wu and Smith 2016; Nakamura et al. 2016; Zhang et al. 2017,
73 2018). It is also consistent with the observed increased frequency of January-February
74 weak polar vortex states in recent decades (Kretschmer et al. 2018). However, the
75 stratospheric response to autumn sea ice loss and its subsequent influence on the wintertime
76 tropospheric response was found to be small compared to the concurrent effect of winter
77 ice loss (Sun et al. 2015; Blackport and Screen 2019). Moreover, atmospheric models
78 forced with observed or projected future Arctic sea ice loss simulate a range of stratospheric
79 polar vortex responses, including weakening (Kim et al. 2014; Nakamura et al. 2016),
80 strengthening (Cai et al. 2012; Scinocca et al. 2009; Screen et al. 2013; Sun et al. 2014;
81 England et al. 2018) and no change (Dai and Song 2020). This range of responses may
82 have many contributing factors, including structural differences among models in their
83 representation of the mean state (Smith et al. 2017) and eddy-mean flow feedbacks (e.g.,
84 Smith et al., 2021), differences in the regional patterns of imposed sea ice loss (Peings and
85 Magnusdottir 2014; Sun et al. 2015; McKenna et al. 2017; Screen 2017), and inadequate

86 sampling of internal variability that obscures the forced response (Seviour 2017). Without
87 modeling consensus, it is difficult to interpret observed relationships between sea ice loss
88 and winter atmospheric circulation (e.g., ice loss in the Barents-Kara Seas and NAO:
89 Peings 2019; Warner et al. 2020).

90 To account for the sources of divergent stratospheric and tropospheric responses among
91 different studies, there is an urgent need for coordinated model experiments. The CMIP6
92 Polar Amplification Model Intercomparison Project (PAMIP) aims to investigate the
93 causes and consequences of polar amplification through a coordinated set of numerical
94 model experiments (Smith et al. 2019). So far, early comparisons have been conducted to
95 address the robustness of sea ice-induced atmospheric circulation change and its underlying
96 mechanisms (Ronald et al. 2020; Smith et al. 2021).

97 As mentioned above, low signal-to-noise ratio is one major obstacle for the detection
98 of an atmospheric circulation response to Arctic sea ice loss (Liang et al. 2020). While
99 some common features of the atmospheric response to projected late 21st century Arctic
100 sea ice loss have been found across models (Screen et al. 2018; Hay et al. 2018; Hay et al.
101 2021), there are substantial discrepancies among modeling studies that consider the
102 response to observed (and thus weaker) Arctic sea ice loss (e.g., Screen et al. 2014). In
103 particular, Sun et al. (2018) investigated the atmospheric circulation response to transient
104 sea ice change from 1990-2090 and found that the forced signal is small compared to the
105 noise from internal variability, especially in the early decades when the ice loss is more
106 limited. To better isolate the signal, a useful approach is to use large ensembles of
107 simulations so as to reduce the noise, in analogy with the initial-condition Large Ensemble
108 framework used in climate change studies (Kay et al. 2015; Maher et al. 2019; Deser et al.

109 2020). In particular, the minimum ensemble size needed to detect a statistically significant
110 atmospheric circulation response signal was found to exceed 50 in the case of observed
111 Arctic sea ice loss (Screen et al. 2014), and 200 according to newer calculations (Labe
112 2020).

113 More recently, Peings et al. (2021; hereafter P21) examined the atmospheric circulation
114 response to future-minus-preindustrial Arctic sea ice loss based on simulations following
115 the PAMIP time-slice protocol with uncoupled and coupled versions of Specified
116 Chemistry-Whole Atmosphere Community Climate Model Version 4 (SC-WACCM4),
117 and found significant inconsistencies among three discrete 100-member ensembles. They
118 identified tropospheric dynamics and ENSO-induced teleconnections as the main sources
119 of internal variability leading to the inconsistencies.

120 This study utilizes the PAMIP time-slice simulations with Community Atmosphere
121 Model version 6 (CAM6) to investigate the effect of Arctic sea ice loss from pre-industrial
122 to present-day, and from present-day to middle 21st century, under two different
123 background SST states. Our study differs from P21 in the following ways. Firstly, we
124 explore role of stratospheric internal variability in the tropospheric response to past and
125 future Arctic sea ice loss, whereas P21 focused on the role of tropospheric internal
126 variability in the response to middle 21st century – minus – preindustrial sea ice loss under
127 a single background SST state. Second, we go beyond the discrete case study approach of
128 P21 by conducting a random sampling bootstrapping procedure to more robustly quantify
129 the spread in tropospheric circulation responses to Arctic sea ice loss arising from internal
130 variability. Third, while P21 and our results both suggest that it is challenging to make
131 causal inferences based on analysis of observations alone due to confounding of internal

132 variability in short (< 50 years) records, our results explicitly highlight the stratospheric
133 pathway which has received much attention in the observational literature.

134 The rest of this paper is organized as follows. Section 2 contains a description of the
135 model and the PAMIP experimental protocol. Section 3 presents results on the relative
136 magnitudes of the stratospheric response to Arctic sea ice loss versus internal variability,
137 the influence of stratospheric internal variability on the tropospheric response to sea ice
138 loss and its mechanism. Section 4 discusses the implications for detection of recent
139 observed trends and model realism. Summary and discussion follow in Section 5.

140

141 **2. Model and Experimental Design**

142 *a. Model description*

143 CAM6 is the atmospheric model component of Community Earth System Model 2
144 (CESM2) developed at the National Center for Atmospheric Research (NCAR). It uses the
145 same Finite Volume (FV) dynamical core as previous versions, but includes the unified
146 turbulence scheme “Cloud Layers Unified By Binormals” (CLUBB; Larson 2017) as well
147 as updates to almost all of the parameterizations (Danabasoglu et al. 2020). CAM6 ranks
148 within the top 10% of the CMIP6 models in representing many features of the atmospheric
149 circulation such as storm tracks, stationary waves and blocking (Simpson et al. 2020).
150 CAM6 has a horizontal resolution of 1.25° in longitude and 0.9° in latitude, and 32 vertical
151 levels with the model top at 2.26 hPa (Danabasoglu et al. 2020). As a “low-top” model, it
152 does not generate a Quasi-Biennial Oscillation (QBO). The SSW frequency in CAM6 is
153 also underestimated (Ayarzaguena et al. 2020), likely resulting from a too strong mean

154 polar vortex. However, as we shall show, the interannual variability of the stratospheric
155 polar vortex and its downward influence on the troposphere are generally realistic.

156

157 *b. PAMIP experimental protocol*

158 We conduct atmosphere-only time slice experiments following PAMIP protocols. In
159 these experiments, the radiative forcing is fixed at year 2000, and sea-surface temperatures
160 (SST) and sea ice concentrations (SIC) are prescribed at preindustrial (pi), present-day (pd)
161 and future (fut) conditions (Smith et al. 2019). The pd SST and SIC are taken from
162 observations, while the pi and fut lower boundary forcings are constructed from the 31
163 historical and Representative Concentration Pathway 8.5 (RCP8.5) simulations
164 respectively from the corresponding 31 Coupled Model Intercomparison Project Phase 5
165 (CMIP5) models (Smith et al. 2019). For each ensemble member, the pi period is defined
166 as the 30 years when the global mean temperature (GMT) equals 13.67 °C, obtaining by
167 removing an estimated global warming index (Haustein et al. 2017) of 0.57 °C from the
168 observed 1979-2008 value (14.24 °C). The fut period is defined as the 30 years when the
169 GMT first exceeds the pi GMT by +2 °C, typically near 2030-2060 (Hausfather 2020).
170 Thus, the magnitude of the sea-ice loss from pd to fut prescribed in PAMIP is substantially
171 smaller than the end of 21st century ice loss commonly used in previous studies (e.g., Screen
172 et al. 2018). The sea ice thickness is set to be uniformly 2 m in the Arctic and 1 m in the
173 Antarctic.

174 Here we conduct the following PAMIP experiments (nomenclature follows that in
175 Table 1 of Smith et al. 2019): 1.1: pdSST-pdSIC; 1.2: piSST-piSIC; 1.3: piSST-pdSIC; 1.4:
176 futSST-pdSIC; 1.5: pdSST-piArcSIC; and 1.6: pdSST-futArcSIC (note that for 1.5 and 1.6,

177 pd SIC is prescribed in the Antarctic). We also conduct an additional experiment: futSST-
 178 futArcSIC (with pd SIC prescribed in the Antarctic). Each simulation starts on April 1st,
 179 2000, initialized from ensemble member 001 of the CAM6 Atmospheric Model
 180 Intercomparison Project (AMIP) historical simulation, and runs for 14 months; we discard
 181 the first 2 months as spin-up from our analysis. For each experiment, we conduct a 200-
 182 member ensemble using the method of “pertlim” (order 10^{-14} K perturbation to the initial
 183 atmospheric temperature field following Kay et al., 2015). Additional details of the PAMIP
 184 protocols and the SST/SIC forcing can be found in Table 1 and Smith et al. (2019).

185 We calculate the atmospheric response to past (pdSIC minus piSIC: Δ_{past}) and future
 186 (futSIC minus pdSIC: Δ_{fut}) Arctic sea ice loss from the 200-member ensemble means of
 187 each experiment as follows:

$$188 \quad \Delta_{\text{past}_{\text{piSST}}} = 1.3 (\text{piSST}-\text{pdSIC}) \text{ minus } 1.2 (\text{piSST}-\text{piSIC}), \quad (1)$$

$$189 \quad \Delta_{\text{past}_{\text{pdSST}}} = 1.1 (\text{pdSST}-\text{pdSIC}) \text{ minus } 1.5 (\text{pdSST}-\text{piArcSIC}), \quad (2)$$

$$190 \quad \Delta_{\text{fut}_{\text{pdSST}}} = 1.6 (\text{pdSST}-\text{futArcSIC}) \text{ minus } 1.1 (\text{pdSST}-\text{pdSIC}), \quad (3)$$

$$191 \quad \Delta_{\text{fut}_{\text{futSST}}} = (\text{futSST}-\text{futArcSIC}) \text{ minus } 1.4 (\text{futSST}-\text{pdSIC}). \quad (4)$$

192 Note that there are two background SST states for the atmospheric circulation responses to
 193 both past and future Arctic sea ice loss. This allows us to investigate whether the responses
 194 are sensitive to the background SST state (e.g., Smith et al. 2017). The False Discovery
 195 Rate (FDR) with control level $\alpha_{\text{FDR}}=0.2$ has been applied to the 90% statistical significance
 196 level on the two-sided Student’s t-test to measure the field significance of the responses
 197 (Wilks 2016).

198

199 *c) Random sampling procedure*

200 The PAMIP protocol recommends a minimum ensemble size of 100 members (Smith
201 et al. 2019). We therefore begin our investigation by examining the sensitivity of the results
202 based on the first 100 members and the second 100 members of our 200-member Δ_{past} and
203 Δ_{fut} ensembles, similar to P21’s approach. The marked differences between these two
204 independent 100-member sub-ensembles leads us to then conduct a more systematic
205 assessment of sampling uncertainty due to internal variability using a random sampling
206 (bootstrapping) procedure (Mudelsee 2010). For each Δ_{past} and Δ_{fut} ensemble, we
207 randomly selected 100 members with replacement from the full 200 members, computed
208 the average of each random 100-member subset, and repeated the entire procedure 1000
209 times. We then used these 1000 random 100-member averages to compute a probability
210 distribution function (PDF) for each of the Δ_{past} and Δ_{fut} ensembles.

211

212 *d) Characterizing stratospheric internal variability*

213 Following convention, we define an index of the strength of the winter (December-
214 February average; DJF) stratospheric polar vortex as the zonal-mean zonal wind at 10 hPa
215 and 60°N (hereafter, U10). We compute U10 for each of the 1000 bootstrapped samples
216 of 100-member averages, and use these to compute PDFs. We also calculate analytical
217 PDFs of 100-member averages of U10 for each of the Δ_{past} and Δ_{fut} ensembles, assuming
218 a Gaussian distribution with mean X_N (equal to the 200-member average) and a standard
219 deviation σ_N :

$$220 \quad \sigma_N = \sigma \cdot \sqrt{\frac{2}{N}}, \quad (5)$$

221 where σ is the standard deviation of U10 across the original 200 members of each ensemble
222 and $N = 100$. The factor of $\sqrt{2}$ accounts for the fact that we are calculating the standard
223 deviation of the difference between a pair of simulations. As shown in Section 3b, the two
224 approaches generate very similar PDFs. Finally, we compute correlation and regression
225 coefficients between U10 and other quantities of interest across the 1000 bootstrapped
226 samples of 100-member averages.

227

228 **3. Results**

229 *a. Surface atmospheric response to past and future Arctic sea ice loss*

230 The loss of Arctic SIC (%) prescribed in the Δ_{past} and Δ_{fut} ensembles occurs mainly
231 within the central Arctic in summer and autumn, and in the marginal ice zones (e.g., Sea
232 of Okhotsk, Bering Sea and Labrador Sea) in winter and spring (Fig. 1a). In the Δ_{fut}
233 ensemble, the SIC reduction in summer and autumn extends all the way to the North Pole
234 (Fig. 1a), with a corresponding increase (up to 140%) in the areal extent of ice loss from
235 July-December compared to the Δ_{past} ensemble (Fig. 1b). The loss of Arctic SIC (%)
236 prescribed in the Δ_{past} and Δ_{fut} ensembles shares regional and seasonal characteristics
237 with observed SIC trends since 1979 (Fig. S1).

238 Sea ice loss results in a net upward energy flux from the ocean to the atmosphere, which
239 in turn is responsible for the near-surface warming over the Arctic and high-latitude
240 continents, as well as the increase in Arctic precipitation (Fig. 2). These responses exhibit
241 similar seasonal cycles, with a minimum in summer and a maximum in winter; note the
242 roughly two-month delay between the peak sea ice loss (October) and the largest

243 atmospheric response (December) for the future ice loss case, in agreement with previous
244 studies (e.g., Deser et al. 2010). The winter surface energy flux and
245 temperature/precipitation responses are approximately twice as large for future ice loss
246 compared to past ice loss, in keeping with the relative magnitudes of sea ice reduction, and
247 show little sensitivity to the background SST conditions, especially for the past ice loss
248 case (Fig. 2). The slightly weaker (~10%) but statistically significant responses for the
249 future ice loss case under future SSTs compared to present-day SSTs is most apparent in
250 October-December (Fig. 2 and S2). It is likely related to enhanced poleward atmospheric
251 energy transport, which warms the Arctic free troposphere (Audette et al. 2021), thus
252 reducing the upward energy transfer from the ocean surface. Outside the Arctic, the
253 atmospheric responses to the same Arctic sea ice loss but under different background SST
254 conditions are largely indistinguishable (not shown). Moreover, internal variability of the
255 surface energy flux response based on 100-member averages is relatively small and thus
256 may not contribute much to the spread in atmospheric response (see error bars in top panel
257 of Fig. 2). In the remainder of this study, we focus on the winter season when the
258 atmospheric response is largest.

259

260 *b. Stratospheric internal variability and its influence on the tropospheric response*

261 To demonstrate the relative magnitudes of the mean stratospheric response to Arctic
262 sea ice loss and its internal variability based on 100-member averages, we show PDFs of
263 the 1000 U10 bootstrapped samples (histograms) along with the analytical distribution
264 (thick black curves) for each of the four ice loss cases in DJF (Fig. 3). The mean U10
265 response of the 1000 100-member averages is -1.6, -0.7, -0.4, and +0.5 m s⁻¹ for $\Delta_{\text{past}_{\text{piSST}}}$,

266 $\Delta\text{past}_{\text{pdSST}}$, $\Delta\text{fut}_{\text{pdSST}}$ and $\Delta\text{fut}_{\text{futSST}}$, respectively. The difference in U10 responses between
267 the two SST states is statistically insignificant for both Δpast and Δfut . In comparison, the
268 standard deviation of the 1000 100-member averages ranges from 1.4 - 1.6 m s^{-1} (similar
269 values obtain for the analytical solution) for all four sea ice cases, indicating a low signal-
270 to-noise ratio for 100-member averages. Due to the low signal-to-noise, by chance, the first
271 and second 100-member averages of U10 (e.g., members 1-100 and 101-200) can differ
272 significantly, as is the case for $\Delta\text{past}_{\text{piSST}}$ (~ -5.2 vs. 1.9 m s^{-1}) and $\Delta\text{fut}_{\text{pdSST}}$ (~ -3.0 vs. 2.3
273 m s^{-1}), or be nearly indistinguishable, as is the case for $\Delta\text{past}_{\text{pdSST}}$ (-0.9 vs. -0.4 m s^{-1}) and
274 $\Delta\text{fut}_{\text{pdSST}}$ (0.5 vs. 0.5 m s^{-1})¹. Since the four sea ice cases have very similar magnitudes of
275 internal variability, these differences highlight the importance of assessing the full
276 distribution via random subsampling rather than relying on two discrete (albeit fully
277 independent) estimates. Indeed, the first and second 100-member averages of U10 for
278 $\Delta\text{past}_{\text{piSST}}$ slightly exceed two standard deviations of the PDF, indicating that they are low
279 probability occurrences. Below, we use this case ($\Delta\text{past}_{\text{piSST}}$) as an example to illustrate
280 how the random sampling of internal stratospheric variability in any 100-member average
281 affects the apparent tropospheric response to Arctic sea ice loss.

282 The vertical structure of the DJF zonal-mean zonal wind response in $\Delta\text{past}_{\text{piSST}}$ based
283 on the full 200-member average shows a statistically significant deceleration of the mean
284 westerlies throughout the troposphere and stratosphere at high latitudes (60-80°N;
285 maximum values around -2.5 m s^{-1} at 10 hPa), and very little response equatorward of 50°N
286 (Fig. 4a). Inspection of the first and second 100-member averages reveals striking

¹ It is noted that there is a very low probability that two of the four cases show significant differences between the first and second 100-member averages. We have exhaustively checked that there were no other underlying reasons for this, and put it down to chance.

287 differences in both the stratosphere and troposphere. The polar vortex weakens
288 substantially in the first 100 members but strengthens in the second 100 members, albeit
289 not significantly (Figs. 4b and c). The tropospheric circulation response in the first 100-
290 member average shows a meridional dipole with deceleration (acceleration) centered at
291 60°N (35°N), resembling the full 200-member average but with larger magnitudes. By
292 contrast, the second 100-member average lacks any statistically significant signal in the
293 extratropical troposphere. These results indicate that using two discrete and independent
294 estimates can lead to non-robustness of atmospheric circulation responses to past and future
295 Arctic sea ice loss in the PAMIP experiments when based on 100 members.

296 It is well-known that NH stratospheric polar vortex is dynamically coupled to the
297 troposphere in boreal winter (e.g., Baldwin et al. 2021). Given that the differences between
298 the first and second 100-member averages span the stratosphere and troposphere, one may
299 surmise that there is a connection between the internal variability in the two domains. To
300 examine this, we plot the monthly evolution of $U(z)$ at 60°N (a proxy for the NAM; Butler
301 et al. 2017) for the first and second 100-member averages and their difference (Fig. 5 a-c).
302 $U(z)$ shows a distinct evolution in the two 100-member averages, consistent with Fig. 4,
303 and their difference is characterized by maximum easterly anomalies peaking in
304 January/February in the stratosphere and February/March at the surface, suggestive of a
305 downward influence.

306 To further explore stratosphere-troposphere coupling more generally, we regress
307 monthly $U(z)$ response at 60°N onto the normalized DJF U10 response across the 1000
308 bootstrapped samples of 100-member averages. We then add or subtract the regression
309 coefficients (multiplied by 2) to the 200-member average to form the 2.5th-to-97.5th

310 percentile confidence intervals on the mean response based on 100-member averages (Figs.
311 5d and e). The results based on regression analysis bear a striking resemblance to the first
312 and second 100-member averages, indicating that most of the difference between the first
313 and second 100-member averages arises from a random, albeit extreme, sampling of
314 stratospheric polar vortex internal variability. Using Pearson correlations in place of
315 regressions reveals a strong connection ($r = 0.5 - 0.6$) between DJF U10 and near-surface
316 U response in January, February and March, lending further support to the conjecture that
317 stratospheric internal variability exerts a substantial influence on the troposphere (Fig. 5g).

318 Figure 6 shows the $\Delta p_{\text{ast}}_{\text{pISST}}$ geopotential height response in the stratosphere (10 hPa
319 in DJF) and troposphere (500 hPa, 850 hPa and 1000 hPa in January-March; JFM) for the
320 first and second 100-member averages and their difference. Consistent with Figs. 4 and 5,
321 the winter polar vortex weakens (consistent with a positive geopotential height anomaly)
322 in the first 100 members but strengthens (consistent with a negative geopotential height
323 anomaly) in the second 100 members. In the troposphere, the first 100-member average
324 shows a barotropic pattern with positive height anomalies over the Arctic and negative
325 height anomalies over North Atlantic midlatitudes, projecting onto the negative phase of
326 the NAO. By contrast, the second 100-member average exhibits a more baroclinic vertical
327 structure in the Nordic Seas, with a negative anomaly near the surface and positive anomaly
328 in the upper levels, similar to the direct response in Deser et al. (2004). The circulation
329 response in the North Pacific is also opposite between the two 100-member averages.

330 Figure 7 shows the corresponding regression maps between U10 and geopotential
331 height based on the 1000 bootstrapped samples of 100-member averages. The patterns in
332 the Mean+2 σ and Mean-2 σ regression maps are largely similar to the first and second 100-

333 member averages, respectively, except over the lower latitude North Pacific (20-40°N). In
334 this region, the difference between the two 100-member averages shows an anomalous
335 ridge which is absent from the regression pattern (Figs. 6c and 7c). In addition, the
336 anomalous trough over the North Atlantic extends further into the Mediterranean Sea in
337 the regression pattern compared to the difference between two sub-ensembles. Overall, the
338 regression pattern (Fig. 7c) closely resembles the NAM throughout the depth of the
339 troposphere, while the difference between the two sub-ensembles exhibits additional
340 regional features (Fig. 6c). The magnitude of the correlation coefficients between U10 and
341 geopotential height across the bootstrapped samples exceeds 0.9 at 10 hPa and reaches 0.6
342 in the troposphere over the main centers of action of the NAM (Fig. S3). Taken together,
343 the results shown in Figs. 5-7 indicate that internal variability of the stratospheric polar
344 vortex exhibits a strong connection to the tropospheric NAM, but that the troposphere also
345 contains its own intrinsic modes of variability.

346 Stratospheric internal variability can also introduce uncertainty in the surface climate
347 response to Arctic sea ice loss estimated from 100-member averages. For example, the
348 pattern and amplitude of the surface air temperature (SAT) response in JFM shows striking
349 differences between the two sub-ensembles of $\Delta\text{past}_{\text{piSST}}$ (Figs. 8a and b; shading). In
350 particular, the second 100-member average exhibits strong and statistically significant
351 warming over northern Eurasia (maximum values exceeding 1.5°C over eastern Siberia),
352 whereas the first 100-member average shows weak and statistically insignificant anomalies
353 of both signs in this region. Notable differences in warming amplitude between the two
354 sub-ensembles are also found over Greenland and northeastern Canada. These SAT
355 differences are clearly linked to the different circulation responses in the two sub-

356 ensembles noted earlier, in particular the opposing SLP responses over the Arctic (contours
357 in Figs. 8a and b). Indeed, the difference between the two sub-ensembles shows evidence
358 of dynamically-induced cooling over northern Eurasia, and warming over eastern Canada
359 and Greenland, in association with the negative NAM-like SLP pattern (Fig. 8c). The
360 regression analysis based on U10 (Mean- 2σ and Mean+ 2σ : Figs. 8d and e) reproduces
361 almost all of the SAT and SLP features seen in the two sub-ensembles, and the difference
362 pattern (Fig. 8f) shows the canonical SAT and SLP signatures associated with a weakened
363 stratospheric polar vortex (e.g., Polvani et al. 2017).

364 Similar to SAT, the JFM precipitation responses in the two sub-ensembles of $\Delta\text{past}_{\text{piSST}}$
365 show striking differences, with opposite-signed meridional dipole patterns over the North
366 Pacific and North Atlantic that result from the opposing circulation responses (Figs. 9a and
367 b). The regression analysis reproduces many of the features of the sub-ensembles over the
368 North Atlantic and Arctic, but shows less agreement over the North Pacific (Figs. 9d and
369 e). This is even more evident in the difference field: the regression analysis strongly
370 underestimates the magnitude of the precipitation and SLP dipoles over the North Pacific,
371 and the North Atlantic SLP trough extends farther to the east, which results in enhanced
372 precipitation over the eastern North Atlantic and Iberian Peninsula, compared to the sub-
373 ensembles (Fig. 9f). These discrepancies highlight that while the stratosphere plays an
374 important role, intrinsic variability of the tropospheric circulation also contributes to
375 uncertainty in the simulated precipitation response to Arctic sea ice loss based on 100-
376 member averages.

377 The influence of stratospheric internal variability on the tropospheric circulation and
378 surface climate responses to Arctic sea ice loss is also apparent for the other sea ice loss

379 cases, based on regression analysis of the bootstrapped samples of 100-member averages
380 (Figs. 10, S4 and S5). Note that for these cases, the first and second 100-member averages
381 do not necessarily mirror the Mean+2 σ and Mean-2 σ regression results, consistent with the
382 chance sampling of U10 documented earlier (Figs. 3 b-d). All cases, however, show a
383 consistent NAM/NAO regression pattern with corresponding fingerprints in SAT and
384 precipitation (panel c in Figs. 10, S4 and S5). Likewise, the pattern and amplitude of the
385 corresponding correlation results are also similar across the 4 cases. In particular, the
386 correlation magnitudes reach ~ 0.6 for SAT in northeastern Siberia and Greenland and for
387 precipitation in Northern Europe and the Mediterranean region (Fig. S6). The consistency
388 of the results across the 4 cases underscores the role of stratospheric internal variability in
389 causing uncertainty in the surface climate response to Arctic sea ice loss when based on
390 100-member averages.

391

392 *c. Mechanism of stratospheric internal variability*

393 Previous studies have established a connection between the strength of the stratospheric
394 polar vortex and upward planetary wave propagation from the troposphere (e.g., Polvani
395 and Waugh 2004), indicating that stratospheric internal variability may originate, at least
396 in part, in the troposphere. To investigate this possible dynamical linkage in $\Delta\text{past}_{\text{pISST}}$, we
397 examine the monthly evolution of the zonal-mean eddy heat flux response near 100 hPa
398 (model 0.1 hybrid sigma level) as a function of latitude in the two 100-member sub-
399 ensembles and the Mean+2 σ and Mean-2 σ regression results (Fig. 11). Consistent with the
400 polar vortex response, the first 100-member average shows increased and statistically
401 significant extratropical upward wave propagation in November-January (NDJ), while the

402 second 100-member average shows insignificant and slightly decreased upward
403 propagation in this season (Figs. 11a and b). Similar results are found in the regression
404 analysis (Fig. 11 d and e). Therefore, the different polar vortex responses between the first
405 and second sub-ensembles (recall Fig. 5a and b) is tied to internal variability of upward
406 wave propagation. Similar results are found for the other sea ice loss cases (Fig. S7).

407 Changes in upward wave propagation have been found to be closely related to
408 interactions between the anomalous and climatological planetary waves (in particular,
409 zonal wave numbers one and two), which has been referred to as the linear wave
410 interference theory (e.g., Garfinkel et al. 2010; Fletcher and Kushner 2011; Smith and
411 Kushner 2012). This suggests that the different responses in upward wave propagation
412 between the first and second 100 member averages of $\Delta\text{past}_{\text{piSST}}$ are also connected to
413 constructive or destructive linear wave interference for zonal wave numbers one and two.
414 Indeed, the NDJ anomalous wave-1 is in phase with its climatology (constructive
415 interference) poleward of 40°N in the first 100-member average, but no such relationship
416 exists in the second 100-member average (Figs. 12a and b). Similarly, while anomalous
417 wave-2 is in quadrature with the climatology in the first 100-member average, it is out of
418 phase with the climatology (destructive interference) in the second 100-member average
419 (Figs. 12 a and b). As a result, there will be more wave-1 and wave-2 upward wave
420 propagation in the first 100-member average than the second. The regression analysis
421 shows similar results regarding wave-1 and wave-2 interference characteristics (Figs. 12d
422 and e), confirming that internally-driven planetary wave interference can largely explain
423 the different upward wave propagation and polar vortex responses in 100-member averages.
424 Similar features can be also seen in the other sea ice loss cases (Figs. S8 and S9), suggesting

425 that this is a universal mechanism connecting internal variability of the stratosphere and
426 troposphere.

427

428 *d. Role of the ensemble size in stratospheric internal variability*

429 While the preceding analysis has focused on 100-member averages, we next investigate
430 the role of ensemble size in determining the magnitude of stratospheric internal variability
431 and its impact on the assessment of the tropospheric response to sea ice loss. To do this,
432 we calculate the 2.5th – 97.5th percentile (-2σ to $+2\sigma$) range of U10 as a function of sample
433 size (number of ensemble members averaged) using the analytical formula in Eqn. 5 for
434 both model and reanalysis. The U10 interannual σ in pdSST-pdSIC (assuming it is
435 equivalent to the standard deviation across 200 ensemble members) is 10.0 m s^{-1} (similar
436 values obtain in the other PAMIP experiments), which is very close to the value of 9.6 m
437 s^{-1} found in the National Centers for Environmental Prediction (NCEP)-NCAR Reanalysis
438 (Kalnay et al. 1996) based on detrended data during 1966-2020 when the data are most
439 reliable (see Fig. S10). Thus, the curves showing the 2.5th – 97.5th percentile ranges of U10
440 response as a function of ensemble size are nearly identical for CAM6 and Reanalysis (Fig.
441 13a). This means that the signal-to-noise ratios of the U10 responses in each of the 4 sea
442 ice loss cases would be similar if the “observed” noise were substituted for the model’s
443 noise. In particular, we note that the 2σ uncertainty based on 200-member averages (2.0
444 m s^{-1} for CAM6, and 1.9 m s^{-1} for Reanalysis; Fig. 13a) exceeds the magnitude of the 200-
445 member averaged U10 response for each of the 4 ice loss cases ($-1.6, -0.7, -0.4, 0.5 \text{ m s}^{-1}$
446 for $\Delta\text{past}_{\text{piSST}}, \Delta\text{past}_{\text{pdSST}}, \Delta\text{fut}_{\text{pdSST}}$ and $\Delta\text{fut}_{\text{futSST}}$, respectively). Thus, our conclusions
447 regarding the effect of stratospheric internal variability on the signal-to-noise of the U10

448 response to ice loss remain valid if using “observed” noise. It should be noted that our
449 estimate of interannual U10 σ reflects internal atmospheric variability only in CAM6,
450 whereas in Reanalysis, coupled ocean-atmosphere and land-atmosphere interactions may
451 also contribute. However, in this regard, we note that the interannual U10 σ in a long pre-
452 industrial control simulation of CAM6 is only 2% smaller than that of the fully-coupled
453 Community Earth System Model version 2 (CESM2).

454 Next, we assess the impact of internal U10 variability on the response of the NAO
455 (normalized PC1 of SLP in the Atlantic-European sector) as a function of sample size based
456 on CAM6 and Reanalysis data. As before, we compute the regression coefficient of the
457 normalized JFM NAO Index onto the normalized DJF U10 Index based on interannual
458 anomalies (detrended in the case of Reanalysis), and use this value in Eqn. 5 (Section 2d).
459 For a sample size of one, the proportion of internal NAO variability associated with U10
460 is slightly smaller for Reanalysis data (1.4) than for the model (1.8), and the difference
461 (scaled by $\frac{1}{\sqrt{N}}$) is maintained for all sample sizes (Fig. 13b). This indicates that either the
462 model overestimates the linkage between the stratospheric polar vortex and the surface
463 NAO, or such linkage is represented correctly in the model but there is just more, unrelated
464 variability in the observations. For the case of a 200-member average, the minimum
465 ensemble size needed for the JFM NAO response in CAM6 to be significantly different
466 from zero at the 95% confidence level is 165, 1296, 144, and 73 for $\Delta\text{past}_{\text{piSST}}$, $\Delta\text{past}_{\text{pdSST}}$,
467 $\Delta\text{fut}_{\text{pdSST}}$ and $\Delta\text{fut}_{\text{futSST}}$, respectively, due to the high level of stratospherically-induced
468 noise in the NAO.

469

470 **4. Implications for attributing observed trends to Arctic sea ice loss**

471 Motivated by empirical observational studies examining the relationship between
472 trends in atmospheric circulation and Arctic warming (or sea ice loss) with inferences about
473 causality (e.g., Francis and Vavrus 2012), we proceed to apply our CAM6 results to the
474 interpretation of observed trends in recent decades. We first note that the “past” sea ice loss
475 adopted for the PAMIP protocol is approximately equivalent to the observed [merged
476 Hadley-Optimum Interpolation (OI) sea ice concentration; Hurrell et al. (2008)] linear
477 change during 1971-2020 for the November-March average (almost identical ice area loss
478 with similar spatial distribution; Fig. S11). Using the analytical approach of Thompson et
479 al. (2015) and Deser et al. (2017), we calculate the 95% margin-of-error (e) on a 50-year
480 linear trend from the statistics of the interannual σ and 1-year lag autocorrelation (r_1) for a
481 Gaussian timeseries as follows. Equation (6) shows the dependence of e on σ and r_1 :

$$482 \quad e = t_c n_t \sigma_{sfc} \gamma(n_t, r_1) g(n_t), \quad (6)$$

483 where $t_c=2$ (95% confidence level), n_t is the length of the trend in years (50), σ_{sfc} is the
484 value of the surface anomaly (SLP, SAT or precipitation) associated with a one σ anomaly
485 of U10, and the other terms are defined as follows.

$$486 \quad \gamma(n_t, r_1) = \left[\frac{n_t - 2}{n_t \left(\frac{1 - r_1}{1 + r_1} \right) - 2} \right]^{\frac{1}{2}}, \quad (7)$$

$$487 \quad g(n_t) = \sqrt{\frac{12}{n_t^3 - n_t}}, \quad (8)$$

488 Figure 14 shows maps of the 95% margin-of-error on a 50-year trend in SLP (top row),
489 SAT (middle row) and precipitation (bottom row) associated with internal variability of
490 the stratospheric polar vortex (U10) based on Reanalysis (first column) and CAM6 (middle
491 column) following the procedure outlined above. Overall, CAM6 shows a realistic
492 depiction of the patterns and magnitudes seen in Reanalysis, including the NAO and its

493 fingerprint on SAT and precipitation. There are some notable differences as well. For
494 example, the observed SLP pattern more closely resembles the regional NAO while the
495 model's pattern is more similar to the hemispheric NAM. As a result, the precipitation
496 values over the North Pacific differ between Reanalysis and CAM6. These discrepancies
497 may be related to the additional influence of El Niño-Southern Oscillation (ENSO) on U10
498 variability in Reanalysis that is lacking in CAM6 due to the use of a climatological seasonal
499 cycle as the SST boundary condition, or it may be a reflection of the well-known bias of
500 atmospheric models to simulate a more zonally-symmetric NAM structure of variability
501 compared to the more regionally-confined NAO structure found in observations (Flato et
502 al. 2013). Over the North Atlantic midlatitudes, the SLP trough is shifted eastward in
503 CAM6 compared to Reanalysis, with impacts on precipitation over the Mediterranean
504 region. This bias appears to be a common issue in climate models (e.g., Sigmond et al.
505 2013; Ayarzagüena et al. 2020).

506 Despite some regional differences in magnitude and pattern, the margin-of-error on the
507 surface climate trends associated with U10 in both CAM6 and Reanalysis substantially
508 exceed the magnitude of the CAM6 response to the observed Arctic sea ice loss trend
509 during 1971-2020, obtained by combining the 200-member averages of $\Delta_{\text{past}_{\text{piSST}}}$ and
510 $\Delta_{\text{past}_{\text{pdSST}}}$ (see above; Fig. 14c). Therefore, unless the model's forced response is
511 substantially underestimated (as some studies suggest: e.g., Mori et al. 2019a) or the model
512 substantially overestimates stratospheric internal variability (e.g., signal-to-noise paradox
513 documented in Smith et al. 2020), it will be difficult to isolate the forced surface climate
514 response to recent Arctic sea ice loss from stratospherically-induced internal variability in
515 observations.

516

517 **5. Summary and discussion**

518 *a. Summary*

519 In this study, we conduct PAMIP time-slice experiments with CAM6 to investigate the
520 atmospheric response to past and projected Arctic sea ice loss, with a specific focus on the
521 role of stratospheric internal variability on the uncertainty in the tropospheric circulation
522 and surface climate response based on 100-member ensembles. Our focus on 100-member
523 averages is motivated by the PAMIP protocol recommendation. We note that increasing
524 the sample size N will reduce the regression magnitudes by a factor of $\frac{1}{\sqrt{N}}$ (Figs. 5f and
525 S12c), but will not affect the correlation magnitudes. Our main findings are summarized
526 as follows.

- 527 1. Consistent with previous studies, the seasonal cycle of the Arctic and terrestrial high-
528 latitude SAT and precipitation responses is approximately in phase with that of the
529 Arctic surface energy flux response, which maximizes in winter (October-March),
530 rather than that of the ice loss, which peaks in autumn (September-October). The
531 internal variability in Arctic surface energy flux response based on 100-member
532 averages is small.
- 533 2. Unlike the surface responses, the magnitude of the winter stratospheric polar vortex
534 response to both past and future Arctic sea ice loss is small compared to its internal
535 variability, even when based on 100-member averages. The stratospheric internal
536 variability is associated with large uncertainty in the tropospheric circulation response
537 to sea ice loss, and can completely obscure the forced NAM/NAO circulation response

538 and associated impacts on air temperatures over Eurasia and eastern North America
539 and precipitation over the North Atlantic and Mediterranean Sea based on 100-member
540 averages.

541 3. Internal variability of the winter stratospheric polar vortex is related to antecedent
542 conditions in tropospheric wave activity. As such, it can be explained by internal
543 variability in upward wave propagation and linear wave interference theory.

544 4. CAM6 exhibits realistic magnitudes of interannual variability in the winter
545 stratospheric polar vortex and its connection to the surface NAO when compared
546 against detrended Reanalysis data during 1966-2020. If the interannual variability of
547 the stratospheric polar vortex is mainly due to internal atmospheric dynamics
548 (including coupling with the troposphere), then Reanalysis data can be used to assess
549 the uncertainty of the atmospheric circulation response to Arctic sea ice loss based on
550 100-member averages following the analytical approach developed by Thompson et al.
551 (2015). The resulting signal-to-noise for the winter (JFM) SLP response to past Arctic
552 sea ice loss is low (< 1) based on 100-member (or 200-member) averages, indicating
553 that unless the model's forced response is substantially underestimated or the model
554 substantially overestimates stratospheric internal variability, it will be difficult to
555 isolate the forced response to recent Arctic sea ice loss in nature.

556

557 *b. Discussion*

558 The results presented above highlight a number of issues. The first one concerns the
559 observed relationship between Arctic sea ice and winter NAO/NAM (e.g., Cohen 2016),
560 which has been hypothesized to reflect a causal influence of Arctic sea ice loss via a

561 stratospheric pathway (Ruggieri et al. 2016) and argued to be one of the dominant climate
562 impacts in recent years (Jaiser et al. 2016). In agreement with Barnes and Screen (2015)
563 and P21, but based on an explicit consideration of the stratospheric pathway, our results
564 caution that empirical analyses that rely on only four decades of observations may face
565 serious sampling issues. Indeed, while Arctic sea ice extent has declined more or less
566 continuously since 1979, the stratospheric polar vortex does not show any significant trend
567 over this time period, but instead exhibits mainly interannual to decadal variability (Fig.
568 S10). Moreover, the observed connection between Arctic sea ice and NAM/NAO has
569 weakened when more recent data (e.g., years 2013-2020) are included in the analysis
570 (Smith et al. 2021), suggesting that part of the relationship may result from stratospheric
571 internal variability and its downward influence on the troposphere.

572 The second issue regards the relative roles of stratospheric versus tropospheric
573 pathways for the forced response to Arctic sea ice loss. When averaged over all 200
574 members, the polar vortex response shows large variation across the four sea ice loss cases
575 (from -1.6 to 0.5 m s^{-1} ; Fig. 3), while the tropospheric circulation responses are quite
576 similar (not shown). Thus, in CAM6, the atmospheric circulation change due to Arctic sea
577 ice loss is mainly dominated by the tropospheric pathway, with a relatively smaller role for
578 the stratospheric pathway. Interestingly, a recent PAMIP multimodel analysis also found
579 divergent stratospheric polar vortex responses but robust tropospheric responses (Smith et
580 al. 2021). Note that these findings do not negate the importance of considering sampling
581 variability in the stratospheric polar vortex response and its impact on the troposphere.

582 The third issue concerns the relative roles of internal variability in the stratosphere
583 versus troposphere. P21 found that the tropospheric circulation, either due to intrinsic

584 atmospheric dynamics or ENSO-related teleconnections, is the main source of internal
585 variability in their PAMIP experiments with SC-WACCM4, while we find that internal
586 variability of the stratospheric polar vortex plays a dominant role in our CAM6 experiments.
587 These results do not contradict each other and can be easily reconciled. As shown in Fig.
588 3, the polar vortex response difference between the first and second 100 members can be
589 large or small solely by chance. When the two 100-member averages show similar U10
590 responses, like in the $\Delta\text{past}_{\text{pdSST}}$ and $\Delta\text{fut}_{\text{futSST}}$ sea ice loss cases, the contribution of internal
591 variability unrelated to the stratosphere will manifest itself in a manner similar to that in
592 P21 (not shown). On the other hand, when the two 100 member-averages of U10 show
593 large differences, as in $\Delta\text{past}_{\text{piSST}}$ and $\Delta\text{fut}_{\text{pdSST}}$, the difference in the tropospheric responses
594 will manifest primarily as an NAO/NAM pattern induced by stratospheric internal
595 variability. More importantly, we have shown that a random selection of 100 members of
596 any of the CAM6 PAMIP sea ice loss experiments is likely to contain substantial
597 stratospheric internal variability, with consequences for the signal-to-noise of the
598 tropospheric and surface climate responses. We note that our results are in agreement with
599 newer PAMIP modeling studies, for example Streffing et al. (2021) who used the Open
600 Integrated Forecasting System, albeit with a focus on the sensitivity to horizontal resolution
601 as opposed to stratospheric internal variability per se. It is also worth mentioning that
602 stratospheric internal variability is not the only source of uncertainty in the tropospheric
603 response to Arctic sea ice loss, but it is substantial (Fig. S13; also inferred from Fig. S6).

604 The fourth issue concerns the mechanisms of stratospheric internal variability. In
605 addition to the eddy heat flux diagnostics (Fig. 11), we also examined the November-
606 January wave activity flux (Plumb 1985) and find very different upward wave propagation

607 responses over Siberia between the two 100-member sub-ensembles, underscoring the
608 important role of tropospheric internal variability in modulating upward wave propagation
609 characteristics through interference with the climatological planetary waves (not shown).
610 Further research is needed to assess additional mechanisms such as troposphere-
611 stratosphere resonance of free modes (Tung and Lindzen, 1979; Plumb, 1981; Esler and
612 Scott, 2005) and interactions between the polar vortex and Aleutian anticyclone (O’Neill
613 and Pope, 1988; Scott and Dritschel, 2006).

614 Our results come with several caveats. CAM6 is a “low-top” model, and as such, it
615 does not internally generate a QBO and thus lacks mechanisms that may be sensitive to the
616 phase of the QBO (e.g., Labe et al. 2019). Although the magnitude of its stratospheric
617 internal variability is realistic (Figures 13 and 14), the mean winter polar vortex is too
618 strong, causing the simulated frequency of sudden stratospheric warmings to be
619 underestimated (Ayarzaguena et al. 2020). It is still unclear whether the stratospheric
620 response to Arctic sea ice loss may depend on the basic state bias in the polar vortex (e.g.,
621 Sigmond et al. 2010; Sun et al. 2015). Finally, our atmosphere-only model experiments do
622 not consider the role of ocean-atmosphere coupling, which has been shown to amplify the
623 response to Arctic sea ice loss (Deser et al. 2016) and expand its reach to the entire globe
624 (e.g., Deser et al., 2015; Tomas et al. 2016; Wang et al., 2018; Peings et al., 2021).

625 Last but not least, it is still an open question whether models underestimate the
626 atmospheric response to Arctic sea ice loss (e.g., Mori et al. 2019a) and associated signal-
627 to-noise ratio (e.g., Smith et al. 2020). So far there is still no consensus (e.g., Screen and
628 Blackport 2019; Mori et al. 2019b), but non-stationarity of the connection between sea ice
629 reduction and atmospheric circulation (Kolstad and Screen 2019; Blackport and Screen

630 2020) appears to imply large internal variability in observations. In other words, the
631 connection may be an artifact of sampling.

632

633 *Acknowledgements*

634 We appreciate the thoughtful comments and suggestions of three anonymous reviewers,
635 and constructive discussions with Dr. Walter A. Robinson (NCSU). NCAR is sponsored
636 by the National Science Foundation. We would like to acknowledge the use of
637 computational resources (doi:10.5065/D6RX99HX) at the NCAR-Wyoming
638 Supercomputing Center provided by the National Science Foundation and the State of
639 Wyoming, and supported by NCAR's Computational and Information Systems Laboratory.

640

641 *Data Availability Statement*

642 The PAMIP data with CAM6 are accessible on the Earth System Grid Federation
643 website (<https://doi.org/10.22033/ESGF/CMIP6.2197>).

644

REFERENCES

645 Ayarzagüena, B., Charlton-Perez, A. J., Butler, A. H., Hitchcock, P., Simpson, I. R.,
646 Polvani, L. M., et al., 2020: Uncertainty in the response of sudden stratospheric warmings
647 and stratosphere-troposphere coupling to quadrupled CO₂ concentrations in CMIP6
648 models. *Journal of Geophysical Research: Atmospheres*, 125, e2019JD032345.
649 <https://doi.org/10.1029/2019JD032345>

650 Audette, A., Fajber, R., Kushner, P., Wu, Y., Peings, Y., Magnusdottir, G., Sigmond, M.,
651 Sun, L., Eade, R., 2021: Opposite responses of the dry and moist eddy heat transport into
652 the Arctic in the PAMIP experiments. *Geophysical Research Letters*,
653 <https://doi.org/10.1029/2020GL089990>.

654 Baldwin, M. P., Ayarzagüena, B., Birner, T., Butchart, N., Butler, A. H., Charlton-Perez,
655 A. J., et al., 2021: Sudden stratospheric warmings. *Reviews of Geophysics*, 59,
656 e2020RG000708. <https://doi.org/10.1029/2020RG000708>.

657 Barnes, E. A., and J. A. Screen, 2015: The impact of Arctic warming on the midlatitude
658 jetstream: Can it? Has it? Will it?, *WIREs Clim. Change*, 6, 277–286.

659 Blackport, R., & Screen, J. A., 2019: Influence of Arctic sea ice loss in autumn compared
660 to that in winter on the atmospheric circulation. *Geophysical Research Letters*, 46, 2213–
661 2221. <https://doi.org/10.1029/2018GL081469>

662 Blackport, R. & J.A. Screen, 2020: Weakened evidence for mid-latitude impacts of Arctic
663 warming. *Nature. Clim. Change*, 10, 1065-1666.

664 Blackport, R., J.A. Screen, K. van der Wiel & R. Bintanja, 2019: Minimal influence of
665 reduced Arctic sea ice on coincident cold winters in mid-latitudes. *Nature Clim. Change*,
666 9, 697-704.

667 Butler, A. H., J. P. Sjoberg, D. J. Seidel, and Karen H. Rosenlof, 2017: A sudden
668 stratospheric warming compendium, *Earth Syst. Sci. Data*, doi:10.5194/essd-9-63-2017.

669 Cai, D., M. Dameris, H. Garny, and T. Runde, 2012: Implications of all season Arctic sea-
670 ice anomalies on the stratosphere. *Atmospheric Chemistry and Physics*, 12, 11819–11831,
671 doi:10.5194/acp-12-11819-2012.

672 Cohen J., 2016: An observational analysis: tropical relative to Arctic influence on
673 midlatitude weather in the era of Arctic amplification. *Geophys Res Lett*, 43:5287–5294.
674 <https://doi.org/10.1002/2016GL069102>.

675 Cohen, J., J. Jones, J.C. Furtado, and E. Tziperman. 2013. Warm Arctic, cold continents:
676 A common pattern related to Arctic sea ice melt, snow advance, and extreme winter
677 weather. *Oceanography* 26(4):150–160, <http://dx.doi.org/10.5670/oceanog.2013.70>.

678 Cohen, J., Zhang, X., Francis, J. et al., 2020: Divergent consensus on Arctic amplification
679 influence on midlatitude severe winter weather. *Nat. Clim. Chang.* 10, 20–29.
680 <https://doi.org/10.1038/s41558-019-0662-y>

681 Dai, A., Song, M., 2020: Little influence of Arctic amplification on mid-latitude climate.
682 *Nat. Clim. Change.* 10, 231–237. <https://doi.org/10.1038/s41558-020-0694-3>

683 Danabasoglu, G., Lamarque, J.-F., Bacmeister, J., Bailey, D. A., DuVivier, A. K., Edwards,
684 J., et al., 2020: The Community Earth System Model Version 2 (CESM2). *Journal of*
685 *Advances in Modeling Earth Systems*, 12, e2019MS001916. [https://doi.org/](https://doi.org/10.1029/2019MS001916)
686 [10.1029/2019MS001916](https://doi.org/10.1029/2019MS001916).

687 Deser, C., F. Lehner, K. B. Rodgers, T. Ault, T. L. Delworth, P. N. DiNezio, A. Fiore, C.
688 Frankignoul, J. C. Fyfe, D. E. Horton, J. E. Kay, R. Knutti, N. S. Lovenduski, J. Marotzke,

689 K. A. McKinnon, S. Minobe, J. Randerson, J. A. Screen, I. R. Simpson and M. Ting, 2020:
690 Insights from earth system model initial-condition large ensembles and future prospects.
691 *Nat. Clim. Change*, doi: 10.1038/s41558-020-0731-2.

692 Deser, C., G. Magnusdottir, R. Saravanan, and A. Phillips, 2004: The effects of North
693 Atlantic SST and sea-ice anomalies on the winter circulation in CCM3, Part II: Direct and
694 indirect components of the response. *J. Climate*, 17, 877-889, doi:10.1175/1520-
695 0442(2004)017<0857:TEONAS>2.0.CO;2.

696 Deser, C., R. A. Tomas, M. A. Alexander, and D. Lawrence, 2010: The Seasonal
697 Atmospheric Response to Projected Arctic Sea Ice Loss in the Late Twenty-First Century.
698 *J. Climate*, 23, 333–351, doi:10.1175/2009JCLI3053.1.

699 Deser, C., R. A. Tomas, and L. Sun, 2015: The role of ocean-atmosphere coupling in the
700 zonal-mean atmospheric response to Arctic sea ice loss. *J. Climate*, 28, 2168-2186, doi:
701 10.1175/JCLI-D-14-00325.1.

702 Deser, C., L. Sun, R. A. Tomas, and J. Screen, 2016: Does ocean coupling matter for the
703 northern extratropical response to projected Arctic sea ice loss?, *Geophys. Res. Lett.*, 43,
704 2149–2157, doi:10.1002/2016GL067792.

705 Deser, Clara, Hurrell, James W., and Phillips, Adam S., 2017, The role of the North
706 Atlantic Oscillation in European climate projections. *Climate Dynamics* Vol. 49, No. 9-10,
707 pp 3141, 1432-0894

708 England, M., Polvani, L., & Sun, L., 2018: Contrasting the Antarctic and Arctic
709 Atmospheric Responses to Projected Sea Ice Loss in the Late Twenty-First Century,
710 *Journal of Climate*, 31(16), 6353-6370. Retrieved Apr 18, 2021, from

711 <https://journals.ametsoc.org/view/journals/clim/31/16/jcli-d-17-0666.1.xml>

712 Esler, J. G., and R. K. Scott (2005), Excitation of transient Rossby waves on the
713 stratospheric polar vortex and the barotropic sudden warming, *J. Atmos. Sci.*, 62, 3661–
714 3682.

715 Fetterer, F., K. Knowles, W. N. Meier, M. Savoie, and A. K. Windnagel. 2017: updated
716 daily. *Sea Ice Index, Version 3*. [sea ice extent]. Boulder, Colorado USA. NSIDC: National
717 Snow and Ice Data Center. doi: <https://doi.org/10.7265/N5K072F8>. [July 16, 2021
718 Accessed].

719 Flato, G., J. Marotzke, B. Abiodun, P. Braconnot, S.C. Chou, W. Collins, P. Cox, F.
720 Driouech, S. Emori, V. Eyring, C. Forest, P. Gleckler, E. Guilyardi, C. Jakob, V. Kattsov,
721 C. Reason and M. Rummukainen, 2013: Evaluation of Climate Models. In: Climate
722 Change 2013: The Physical Science Basis. Contribution of Working Group I to the Fifth
723 Assessment Report of the Intergovernmental Panel on Climate Change [Stocker, T.F., D.
724 Qin, G.-K. Plattner, M. Tignor, S.K. Allen, J. Boschung, A. Nauels, Y. Xia, V. Bex and
725 P.M. Midgley (eds.)]. Cambridge University Press, Cambridge, United Kingdom and New
726 York, NY, USA.

727 Fletcher, C. G. and P. J. Kushner, 2011: The Role of Linear Interference in the Annular
728 Mode Response to Tropical SST Forcing. *J. Climate*, 24, 778-794.

729 Francis, J. A., and S. J. Vavrus, 2012: Evidence linking Arctic amplification to extreme
730 weather in mid-latitudes, *Geophys. Res. Lett.*, 39, L06801, doi:10.1029/2012GL051000.

731 Garfinkel, C. I., D. L. Hartmann, and F. Sassi, 2010: Tropospheric Precursors of

732 Anomalous Northern Hemisphere Stratospheric Polar Vortices. *J. Climate*, 23, 3282-3299.

733 Hausfather, Zeke, 2020: Analysis: When might the world exceed 1.5°C and 2°C of global
734 warming? World economy forum, last accessed on June 2, 2021 at
735 [https://www.weforum.org/agenda/2020/12/analysis-world-paris-agreement-climate-](https://www.weforum.org/agenda/2020/12/analysis-world-paris-agreement-climate-targets-change-emissions-global-warming/)
736 [targets-change-emissions-global-warming/](https://www.weforum.org/agenda/2020/12/analysis-world-paris-agreement-climate-targets-change-emissions-global-warming/)

737 Haustein, K., M. R. Allen, P. M. Forster, F. E. L. Otto, D. M. Mitchell, H. D. Matthews
738 and D. J. Frame, 2017: A real-time Global Warming Index, *Scientific Reports*, 7, 15417,
739 doi:10.1038/s41598-017-14828-5.

740 Hay, S., P. Kushner, R. Blackport and K. McCusker, 2018: On the relative robustness of
741 the atmospheric circulation response to high-latitude and low-latitude warming, *Geophys.*
742 *Res. Lett.*, <https://doi.org/10.1029/2018GL077294>.

743 Hay, S., P. Kushner, R. Blackport, K. McCusker, T. Oudar, L. Sun, M. England, C. Deser,
744 J. Screen and L. Polvani, 2021: Separating the influences of low-latitude warming and sea-
745 ice loss on Northern Hemisphere climate change, *Journal of Climate*, in revision.

746 Hurrell, J. W., 1995: Decadal trends in the North Atlantic Oscillation: Regional
747 temperatures and precipitation. *Science*, 269, 676-679.

748 Hurrell, James W., James J. Hack, Dennis Shea, Julie M. Caron, James Rosinski, 2008: A
749 New Sea Surface Temperature and Sea Ice Boundary Dataset for the Community
750 Atmosphere Model. *J. Climate*, 21, 5145–5153. doi: 0.1175/2008JCLI2292.1.

751 Jaiser, Ralf, K. Dethloff and D. Handorf, 2013: Stratospheric response to Arctic sea ice
752 retreat and associated planetary wave propagation changes. 65. *Tellus A*, doi:

753 <http://dx.doi.org/10.3402/tellusa.v65i0.19375>.

754 Jaiser, R., Nakamura, T., Handorf, D., Dethloff, K., Ukita, J., and Yamazaki, K., 2016:
755 Atmospheric winter response to Arctic sea ice changes in reanalysis data and model
756 simulations, *J. Geophys. Res. Atmos.*, 121, 7564–7577, doi:10.1002/2015JD024679.

757 Kalnay, E., Kanamitsu, M., Kistler, R., Collins, W., Deaven, D., Gandin, L., Iredell, M.,
758 Saha, S., White, G., Woollen, J., Zhu, Y., Chelliah, M., Ebisuzaki, W., Higgins, W.,
759 Janowiak, J., Mo, K. C., Ropelewski, C., Wang, J., Leetmaa, A., Reynolds, R., Jenne, R.,
760 & Joseph, D., 1996: The NCEP/NCAR 40-Year Reanalysis Project, *Bulletin of the*
761 *American Meteorological Society*, 77(3), 437-472.

762 Kay, J. E., Deser, C., Phillips, A., Mai, A., Hannay, C., Strand, G., Arblaster, J., Bates, S.,
763 Danabasoglu, G., Edwards, J., Holland, M. Kushner, P., Lamarque, J.-F., Lawrence, D.,
764 Lindsay, K., Middleton, A., Munoz, E., Neale, R., Oleson, K., Polvani, L., and M.
765 Vertenstein, 2015: The Community Earth System Model (CESM) Large Ensemble Project:
766 A Community Resource for Studying Climate Change in the Presence of Internal Climate
767 Variability, *Bulletin of the American Meteorological Society*, doi: 10.1175/BAMS-D-13-
768 00255.1

769 Kim, B.-M., S.-W. Son, S.-K. Min, J.-H. Jeong, S.-J. Kim, X. Zhang, T. Shim, and J.-H.
770 Yoon, 2014: Weakening of the stratospheric polar vortex by Arctic sea-ice loss. *Nature*
771 *communications*, 5, 4646, doi:10.1038/ncomms5646.

772 Kolstad E. W. and J. A. Screen, 2019: Nonstationary relationship between autumn Arctic
773 sea ice and the winter North Atlantic oscillation. *Geophysical Research Letters*, 46, 7583–
774 7591. <https://doi.org/10.1029/2019GL083059>.

775 Kretschmer, M. et al., 2018: More frequent weak stratospheric polar vortex states linked to
776 mid-latitude cold extremes. *Bull. Am. Meteorol. Soc.* 99, 49–60 (2018).

777 Labe, Z. M., Y. Peings, and G. Magnusdottir, 2019: The effect of QBO phase on the
778 atmospheric response to projected Arctic sea ice loss in early winter. *Geophysical Research*
779 *Letters*, DOI:10.1029/2019GL083095

780 Labe, Z. M., 2020: The effects of Arctic sea-ice thickness loss and stratospheric variability
781 on mid-latitude cold spells. University of California, Irvine. Doctoral Dissertation.

782 Larson, V. E., 2017: CLUBB-SILHS: A parameterization of subgrid variability in the
783 atmosphere. arXiv:1711.03675v2 [physics.ao-ph].

784 Liang, Y.-C., Y.-O. Kwon, C. Frankignoul, G. Danabasoglu, S. Yeager, A. Cherchi, Y.
785 Gao, G. Gastineau, R. Ghosh, D. Matei, J. V. Mecking, D. Peano, L. Suo, and T. Tian,
786 2019: Quantification of the Arctic sea ice-driven atmospheric circulation variability in
787 coordinated large ensemble simulations, *Geophysical Research Letters*, 47,
788 doi:1029/2019GL085397

789 Maher, N., Milinski, S., Suarez- Gutierrez, L., Botzet, M., Dobrynin, M., Kornblueh, L., et
790 al., 2019: The Max Planck Institute Grand Ensemble: Enabling the exploration of climate
791 system variability. *Journal of Advances in Modeling Earth Systems*, 11, 2050–2069.
792 <https://doi.org/10.1029/2019MS001639>

793 McCusker, Kelly E., J. C. Fyfe, M. Sigmond, 2016: Twenty-five winters of unexpected
794 Eurasian cooling unlikely due to Arctic sea ice loss, *Nature Geoscience*,

795 doi:10.1038/ngeo2820.

796 McKenna, C. M., Bracegirdle, T. J., Shuckburgh, E. F., Haynes, P. H., & Joshi, M. M.,
797 2018: Arctic sea ice loss in different regions leads to contrasting Northern Hemisphere
798 impacts. *Geophysical Research Letters*, 45, 945–954.
799 <https://doi.org/10.1002/2017GL076433>

800 Mori, M., M. Watanabe, H. Shiogama, J. Inoue, and M. Kimoto, 2014: Robust arctic sea-
801 ice influence on the frequent Eurasian cold winters in past decades. *Nature Geoscience*, 7,
802 869–873, doi:10.1038/ngeo2277.

803 Mori, M., Kosaka, Y., Watanabe, M., Nakamura, H. & Kimoto, M., 2019a: A reconciled
804 estimate of the influence of Arctic sea-ice loss on recent Eurasian cooling. *Nat. Clim.*
805 *Change* 9, 123–129.

806 Mori, M., Kosaka, Y., Watanabe, M. et al., 2019b: Reply to: Is sea-ice-driven Eurasian
807 cooling too weak in models?. *Nat. Clim. Chang.* 9, 937–939.
808 <https://doi.org/10.1038/s41558-019-0636-0>

809 Mudelsee M, 2010: *Climate Time Series Analysis: Classical Statistical and Bootstrap*
810 *Methods*. First edition. Springer, Dordrecht, 474pp

811 Nakamura T, Yamazaki K, Iwamoto K, Honda M, Miyoshi Y, Ogawa Y, Tomikawa Y,
812 Ukita J, 2016: The stratospheric pathway for Arctic impacts on midlatitude climate.
813 *Geophys Res Lett* 43:3494–3501. <https://doi.org/10.1002/2016GL068330>

814 Notz, D., & SIMIP Community, 2020: Arctic sea ice in CMIP6. *Geophysical Research*

815 *Letters*, 47, e2019GL086749. <https://doi.org/10.1029/2019GL086749>.

816 Ogawa, F., and Coauthors, 2018: Evaluating impacts of recent Arctic sea ice loss on the
817 Northern Hemisphere winter climate change. *Geophys. Res. Lett.*, 45, 3255–3263,
818 <https://doi.org/10.1002/2017GL076502>.

819 O'Neill, A., and V. D. Pope (1988), Simulations of linear and nonlinear disturbances in the
820 stratosphere, *Q. J. R. Meteorol. Soc.*, 114, 1063–1110.

821 Overland, J. E., Wood, K. R., M. Wang, 2011: Warm Arctic-cold continents: Climate
822 impacts of the newly open arctic sea. *Polar Research*, 30(SUPPL.1), 1–14.
823 <http://doi.org/10.3402/polar.v30i0.15787>.

824 Peings, Y. and G. Magnusdottir, 2014: Response of the Wintertime Northern Hemisphere
825 Atmospheric Circulation to Current and Projected Arctic Sea Ice Decline: A Numerical
826 Study with CAM5. *J. Climate*, 27, 244–264, doi: 10.1175/JCLI-D-13-00272.1.

827 Peings, Y., 2019: Ural blocking as a driver of early-winter stratospheric warmings.
828 *Geophysical Research Letters*, 46, 5460–5468. <https://doi.org/10.1029/2019GL082097>.

829 Peings, Y., Z.M. Labe, and G. Magnusdottir, 2021: Are 100 ensemble members enough to
830 capture the remote atmospheric response to +2°C Arctic sea ice loss? *Journal of Climate*,
831 DOI:10.1175/JCLI-D-20-0613.1

832 Perlwitz, J., M. Hoerling, and R. Dole, 2015:, Arctic tropospheric warming: Causes and
833 linkages to lower latitudes. *J. Climate*, 28, 2154–2167, [https://doi.org/10.1175/JCLI-D-14-](https://doi.org/10.1175/JCLI-D-14-00095.1)
834 00095.1.

835 Plumb, R. A. (1981), Instability of the distorted polar night vortex: A theory of
836 stratospheric warmings, *J. Atmos. Sci.*, 38, 2514– 2531.

837 Polvani, L., Sun, L., Butler, A. H., Richter, J. H., & Deser, C., (2017: Distinguishing
838 stratospheric sudden warmings from ENSO as key drivers of wintertime climate variability
839 over the North Atlantic and Eurasia, *J. Climate*, 30(6), 1959-1969.
840 <https://doi.org/10.1175/JCLI-D-16-0277.1>

841 Polvani, L. M. and D. W. Waugh, 2004: Upward wave activity flux as precursor to extreme
842 stratospheric events and subsequent anomalous surface weather regimes. *J. Climate*, 17,
843 3548–3554.

844 Ronalds B., E.A. Barnes, R. Eade, Y. Peings, M. Sigmond, 2020: North Pacific zonal wind
845 response to sea ice loss in the Polar Amplification Model Intercomparison Project and its
846 downstream implications. *Climate Dynamics*, [https://doi.org/10.1007/s00382-020-05352-](https://doi.org/10.1007/s00382-020-05352-w)
847 [w](https://doi.org/10.1007/s00382-020-05352-w)

848 Ruggieri, P., R. Buizza, and G. Visconti, 2016: On the link between Barents-Kara sea ice
849 variability and European blocking, *J. Geophys. Res. Atmos.*, 121, 5664–5679,
850 [doi:10.1002/2015JD024021](https://doi.org/10.1002/2015JD024021).

851 Scinocca, J. F., M. C. Reader, D. A. Plummer, M. Sigmond, P. J. Kushner, T. G. Shepherd,
852 and R. Ravishankara, 2009: Impact of sudden Arctic sea-ice loss on stratospheric polar
853 ozone *Geophys. Res. Lett.*, 36, L24701, [doi:10.1029/2009GL041239](https://doi.org/10.1029/2009GL041239).

854 Scott, R. K., and D. G. Dritschel (2006), Vortex-vortex interactions in the winter
855 stratosphere, *J. Atmos. Sci.*, 63, 726–740.

856 Screen, J. A., 2017: Simulated atmospheric response to regional and pan-Arctic sea ice loss.
857 *Journal of Climate*, 30, 3945–3962. <https://doi.org/10.1175/JCLI-D-16-0197.1>.

858 Screen, J.A. & R. Blackport, 2019: Is sea-ice-driven Eurasian cooling too weak in models?
859 *Nature Clim. Change*, 9, 934-936.

860 Screen, J. A., C. Deser, I. Simmonds, and R. Tomas, 2014: Atmospheric impacts of Arctic
861 sea-ice loss, 1979-2009: Separating forced change from atmospheric internal variability.
862 *Clim. Dyn.*, 43, 333-344., doi: 10.1007/s00382-013-1830-9.

863 Screen J., C. Deser, D. M. Smith, X. Zhang, R. Blackport, P. J. Kushner, T. Oudar, K. E.
864 McCusker and L. Sun, 2018: Consistency and discrepancy in the atmospheric response to
865 Arctic sea ice loss across climate models, *Nature Geoscience*, doi:10.1038/s41561-018-
866 0059-y.

867 Screen, J. a. and I. Simmonds, 2010: The central role of diminishing sea ice in recent Arctic
868 temperature amplification. *Nature*, 464, 1334–7, doi:10.1038/nature09051.

869 Screen, J. a., I. Simmonds, C. Deser, and R. Tomas, 2013: The Atmospheric Response to
870 Three Decades of Observed Arctic Sea Ice Loss. *J. Climate*, 26, 1230–1248,
871 doi:10.1175/JCLI-D-12-00063.1.

872 Seviour, W. J. M., 2017: Weakening and shift of the Arctic stratospheric polar vortex:
873 Internal variability or forced response?, *Geophys. Res. Lett.*, 44, 3365– 3373,
874 doi:10.1002/2017GL073071.

875 Sigmond, M. and J. F. Scinocca, 2010: The Influence of Basic State on the Northern
876 Hemisphere Circulation Response to Climate Change. *J. Climate*, 23, 1434–1446.

877 Sigmond, M., J. F. Scinocca, V.V. Kharin, T.G. Shepherd, 2013: Enhanced seasonal
878 forecast skill following stratospheric sudden warmings, *Nature Geosci.*, 6, 98-102.

879 Simpson, I. R., Bacmeister, J., Neale, R. B., Hannay, C., Gettelman, A., Garcia, R. R., et
880 al., 2020: An evaluation of the large-scale atmospheric circulation and its variability in
881 CESM2 and other CMIP models. *Journal of Geophysical Research: Atmospheres*, 125,
882 e2020JD032835. [https://doi.org/ 10.1029/2020JD032835](https://doi.org/10.1029/2020JD032835)

883 Smith, D. M., Nick J. Dunstone, Adam A. Scaife, Emma K. Fiedler, Dan Copsey, and
884 Steven C. Hardiman, 2017: Atmospheric Response to Arctic and Antarctic Sea Ice: The
885 Importance of Ocean–Atmosphere Coupling and the Background State. *Journal of Climate*,
886 30:12, 4547-4565.

887 Smith, D.M., Scaife, A.A., Eade, R. et al., 2020: North Atlantic climate far more
888 predictable than models imply. *Nature* 583, 796–800. [https://doi.org/10.1038/s41586-020-](https://doi.org/10.1038/s41586-020-2525-0)
889 2525-0.

890 Smith, D. M., Screen, J. A., Deser, C., Cohen, J., Fyfe, J. C., García-Serrano, J., Jung, T.,
891 Kattsov, V., Matei, D., Msadek, R., Peings, Y., Sigmond, M., Ukita, J., Yoon, J.-H., and
892 Zhang, X., 2019: The Polar Amplification Model Intercomparison Project (PAMIP)
893 contribution to CMIP6: investigating the causes and consequences of polar amplification,
894 *Geosci. Model Dev.*, 12, 1139-1164, <https://doi.org/10.5194/gmd-12-1139-2019>.

895 Smith, D. M., R. Eader, M. Andrews, H. Ayres, A. Clark, S. Chripko, C. Deser, N. J.
896 Dunstone, J. Garcia-Serrano, G. Gastineau, L. S. Graff, S. Hardiman, B. He, L. Hermanson,
897 T. Jung, J. Knight, X. Levine, G. Magnusdottir, E. Manzini, D. Matei, M. Mori, R. Msadek,

898 P. Ortega, Y. Peings, A. A. Scaife, J. A. Screen, T. Semmler, M. Sigmond, J. Streffing, L.
899 Sun, A. Walsh, 2021: Observationally constrained multi-model ensemble atmospheric
900 response to future Arctic sea ice loss, *Nature communication*, in review.

901 Smith, K. L. and P. J. Kushner, 2012: Linear interference and the initiation of extratropical
902 stratosphere-troposphere interactions. *Journal of Geophysical Research*, 117, D13107,
903 doi:10.1029/2012JD017587.

904 Streffing, J., Semmler, T., Zampieri, L., & Jung, T. (2021). Response of Northern
905 Hemisphere Weather and Climate to Arctic Sea Ice Decline: Resolution Independence in
906 Polar Amplification Model Intercomparison Project (PAMIP) Simulations, *Journal of*
907 *Climate*, 34(20), 8445-8457.

908 Sun, L., Alexander, M. A., & Deser, C., 2018: Evolution of the global coupled climate
909 response to Arctic sea ice loss during 1990-2090 and its contribution to climate change.
910 *Journal of Climate*, 31(19), 7823–7843. <https://doi.org/10.1175/JCLI-D-18-0134.1>.

911 Sun, L., C. Deser, L. M. Polvani, and R. Tomas, 2014: Influence of projected Arctic sea
912 ice loss on polar stratospheric ozone and circulation in spring. *Environmental Research*
913 *Letters*, 9, 084016, doi:10.1088/1748-9326/9/8/084016.

914 Sun, L., C. Deser and R. A. Tomas, 2015: Mechanisms of stratospheric and tropospheric
915 circulation response to projected Arctic sea ice loss, *J. Climate*, 28, 7824–7845. doi:
916 <http://dx.doi.org/10.1175/JCLI-D-15-0169.1>.

917 Sun, L., J. Perlwitz and M. Hoerling, 2016: What caused the recent "Warm Arctic, Cold

918 Continents" trend pattern in winter temperatures? *Geophys. Res. Lett.*, doi:
919 <http://dx.doi.org/10.1002/2016GL069024>.

920 Thompson, D. W. J. and J. M. Wallace, 2000: Annular Modes in the Extratropical
921 Circulation. Part I: Month-to-Month Variability. *J. Climate*, 13, 1000–1016.

922 Thompson, D. W. J., Barnes, E. A., Deser, C., Foust, W. E., & Phillips, A. S., 2015:
923 Quantifying the Role of Internal Climate Variability in Future Climate Trends, *Journal of*
924 *Climate*, 28(16), 6443-6456.

925 Tomas, R. A., C. Deser, and L. Sun, 2016: The role of ocean heat transport in the global
926 climate response to projected Arctic sea ice loss. *J. Climate*, 29, 6841–6859,
927 <https://doi.org/10.1175/JCLI-D-15-0651.1>.

928 Tung, K. K., and R. S. Lindzen (1979), A theory of stationary long waves. Part I: A simple
929 theory of blocking, *Mon. Weather Rev.*, 107, 714–734.

930 Wang, K., C. Deser, L. Sun, and R. Tomas, 2018: Fast response of the tropics to an abrupt
931 loss of Arctic sea ice via ocean dynamics. *Geophys. Res. Lett.*, 45, 4264–4272,
932 <https://doi.org/10.1029/2018GL077325>.

933 Warner, J.L., J.A. Screen & A.A. Scaife, 2020: Links between Barents-Kara sea ice and
934 the extratropical atmospheric circulation explained by internal variability and tropical
935 forcing. *Geophys. Res. Lett.*, 47, e2019GL085679.

936 Wilks, D. S., 2016: "The stippling shows statistically significant grid points": How research
937 results are routinely overstated and overinterpreted, and what to do about it. *Bull. Amer.*
938 *Meteor. Soc.*, 97, 2263-22.

939 Wu, Y. and K. L. Smith, 2016: Response of Northern Hemisphere Midlatitude Circulation
940 to Arctic Amplification in a Simple Atmospheric General Circulation Model. *J. Clim.*, 29,
941 2041-2058.

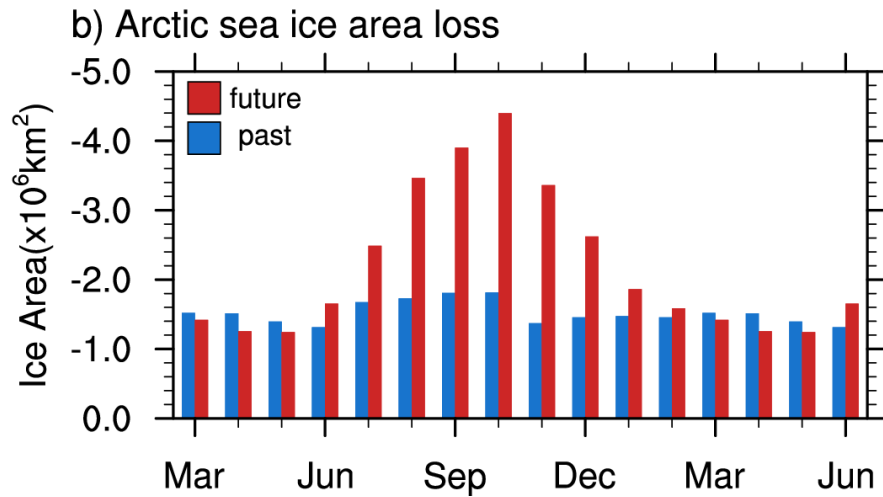
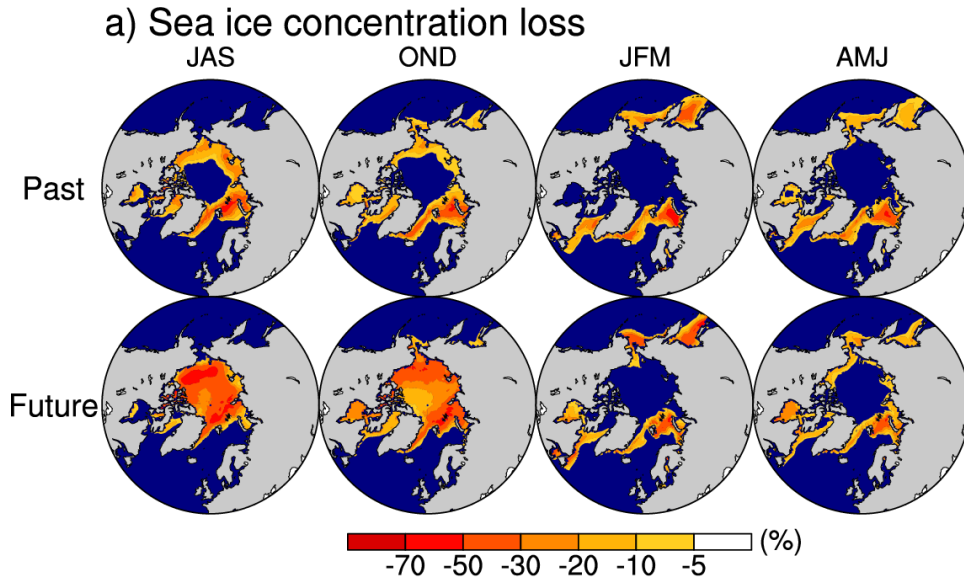
942 Zhang, P., Wu, Y. and K. L. Smith, 2017: Prolonged Effect of the Stratospheric Pathway
943 in Linking Barents-Kara Sea Sea Ice Variability to the Midlatitude Circulation in a
944 Simplified Model. *Clim. Dyn.*, <https://doi.org/10.1007/s00382-017-3624-y>.

945 Zhang, P., Wu, Y., Simpson, I. R., Smith, K. L., Zhang, X., De, B., & Callaghan, P., 2018:
946 A stratospheric pathway linking a colder Siberia to Barents-Kara Sea sea ice loss. *Science*
947 *Advances*, 4(7), eaat6025. 915 <https://doi.org/10.1126/sciadv.aat6025>

948 **Table 1.** PAMIP atmosphere-only time-slice experiments conducted in this study using
 949 Community Atmosphere Model version 6 (see text for details of the experimental design).
 950 Nomenclature follows that in Smith et al. (2019).

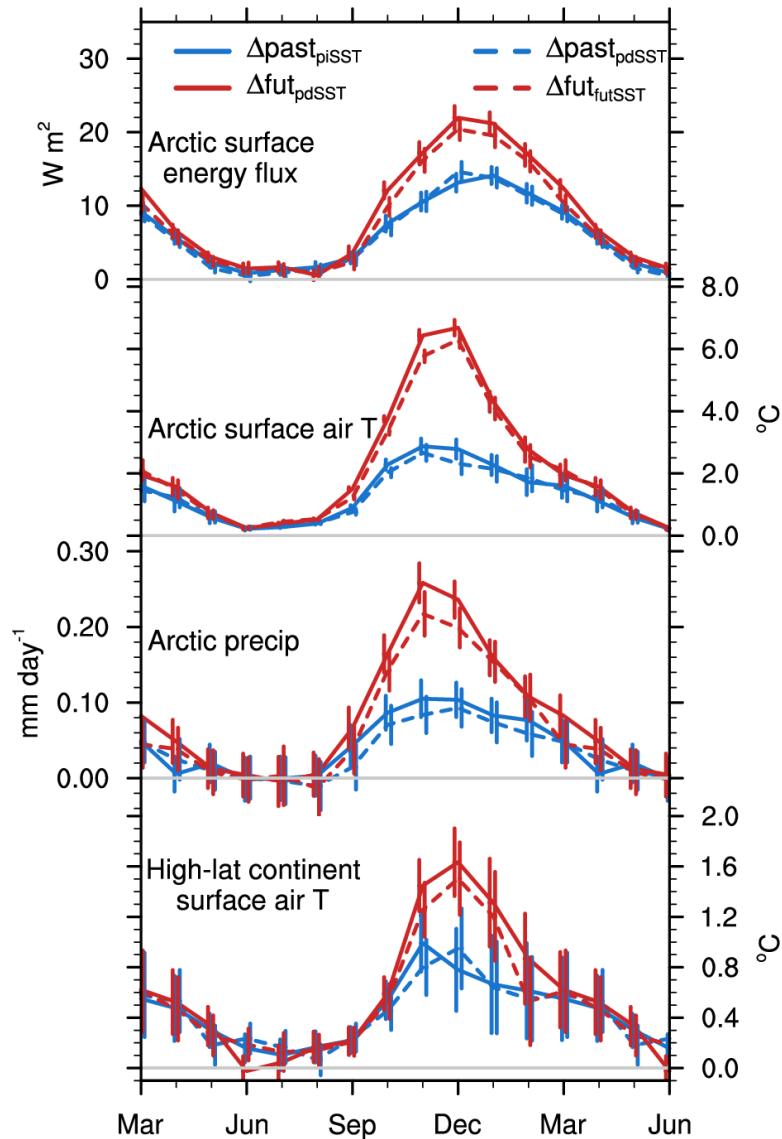
No.	Experiment name	SST forcing	SIC forcing	Other details
1.1	pdSST-pdSIC	present-day conditions	present-day conditions	Year-2000 radiative forcing; 14-month time-slice run with the first 2 months discarded as spin-up; ensemble size of 200; set ice thickness set to be 2 m in the Arctic and 1 m in the Antarctic
1.2	piSST-piSIC	preindustrial conditions	preindustrial conditions	
1.3	piSST-pdSIC	preindustrial conditions	present-day conditions	
1.4	futSST-pdSIC	future conditions	present-day conditions	
1.5	pdSST-piArcSIC	present-day conditions	preindustrial conditions in the Arctic, present-day conditions in the Antarctic	
1.6	pdSST-futArcSIC	present-day conditions	future conditions in the Arctic, present-day conditions in the Antarctic	
	futSST-futArcSIC	future conditions	future conditions in the Arctic, present-day conditions in the Antarctic	

951



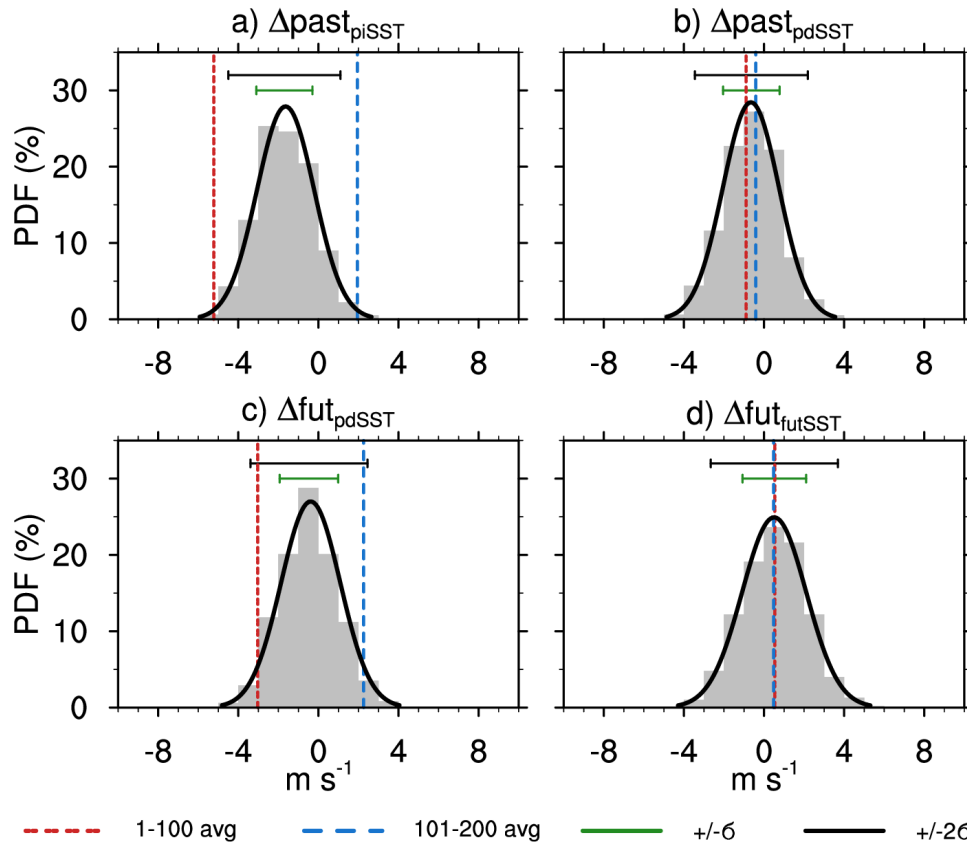
952

953 **Figure 1.** (a) Seasonal maps of prescribed Arctic SIC loss (%) in the PAMIP experiments
 954 for the past (preindustrial to present-day) and future (present-day to +2°C warming above
 955 preindustrial level). Summer, autumn, winter and spring seasons are defined to be the
 956 average of July-September (JAS), October-December (OND), January-March (JFM) and
 957 April-June (AMJ), respectively. (b) Monthly Arctic sea ice area loss (10^6 km^2) for the past
 958 (blue) and future (red); note the inverted y-axis scale.
 959



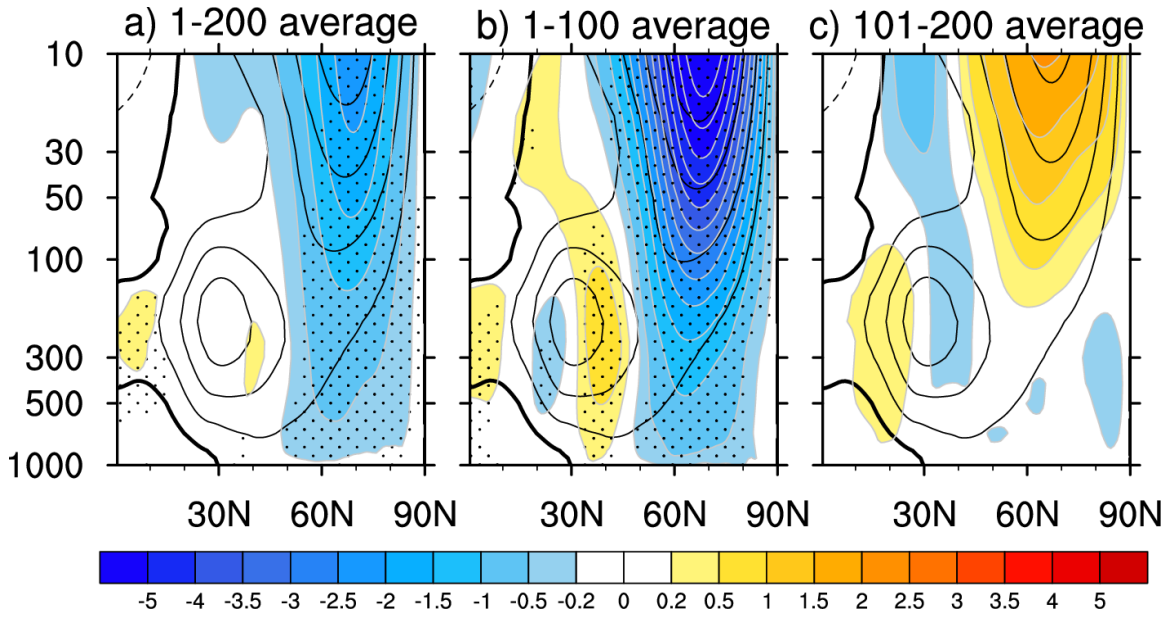
960
 961
 962
 963
 964
 965
 966
 967
 968
 969
 970
 971
 972

Figure 2. Monthly responses to past (blue) and future (red) Arctic sea ice loss for (from top to bottom): Arctic net upward surface energy flux ($W m^{-2}$; positive upward); Arctic surface air temperature ($^{\circ}C$); Arctic precipitation ($mm day^{-1}$); and high-latitude (poleward of $50^{\circ}N$) terrestrial surface air temperature ($^{\circ}C$). The surface energy flux is the sum of the turbulent (sensible plus latent) heat flux and the long-wave radiative flux. Solid and dashed blue curves indicate the past sea ice loss with preindustrial and present-day background SSTs, while solid and dashed red curves indicate the future sea ice loss with present-day and future background SSTs. The Arctic responses are averaged over all grid boxes containing a minimum of 15% present-day climatological SIC in March. Vertical line segments show the two standard deviation error bars based on the bootstrapped 100-member averages (see text for details).



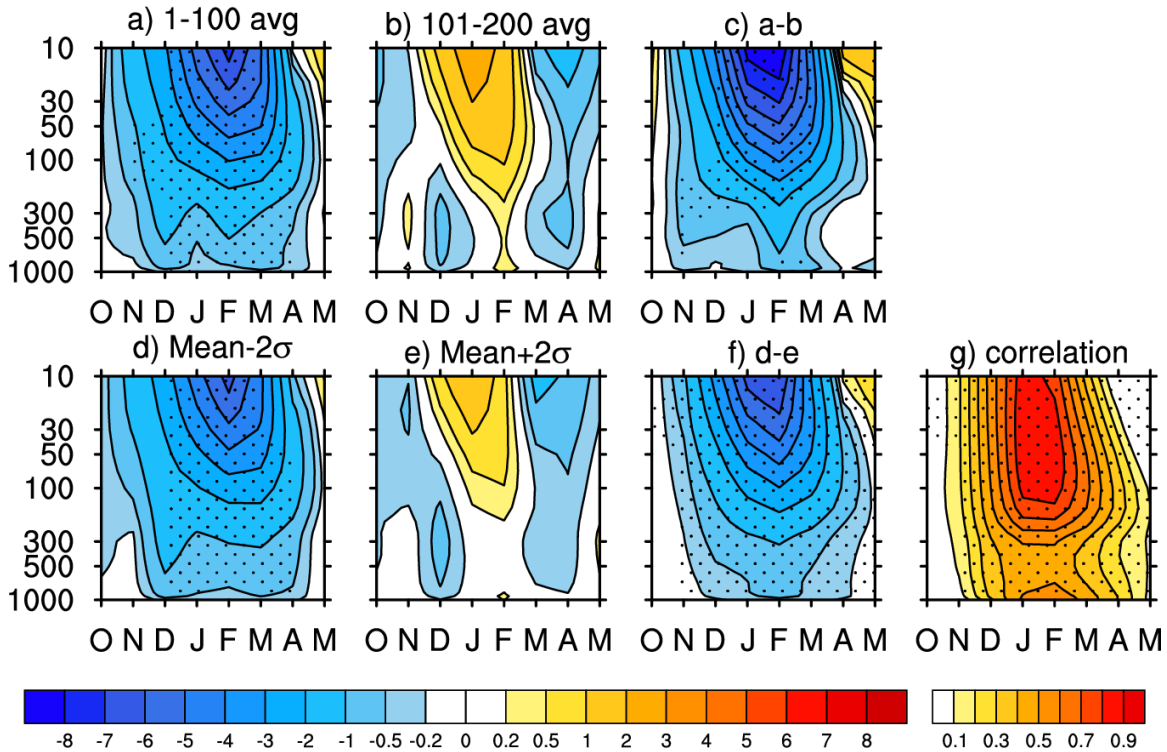
973
974

975 **Figure 3.** Probability density function (PDF) of 100-member averages of DJF U10 for: (a)
 976 $\Delta\text{past}_{\text{piSST}}$; (b) $\Delta\text{past}_{\text{pdSST}}$; (c) $\Delta\text{fut}_{\text{pdSST}}$ and (d) $\Delta\text{fut}_{\text{futSST}}$. For each case, the histogram is
 977 evaluated by randomly selecting 100 members with replacement from the 200-member
 978 ensembles and repeating this procedure 1000 times. Curves are calculated analytically from
 979 the interannual standard deviation (see text). Horizontal green (black) bar indicates +/- one
 980 (two) standard deviations of the PDF. Vertical dashed red (blue) line indicates the average
 981 over the first (second) 100 members.



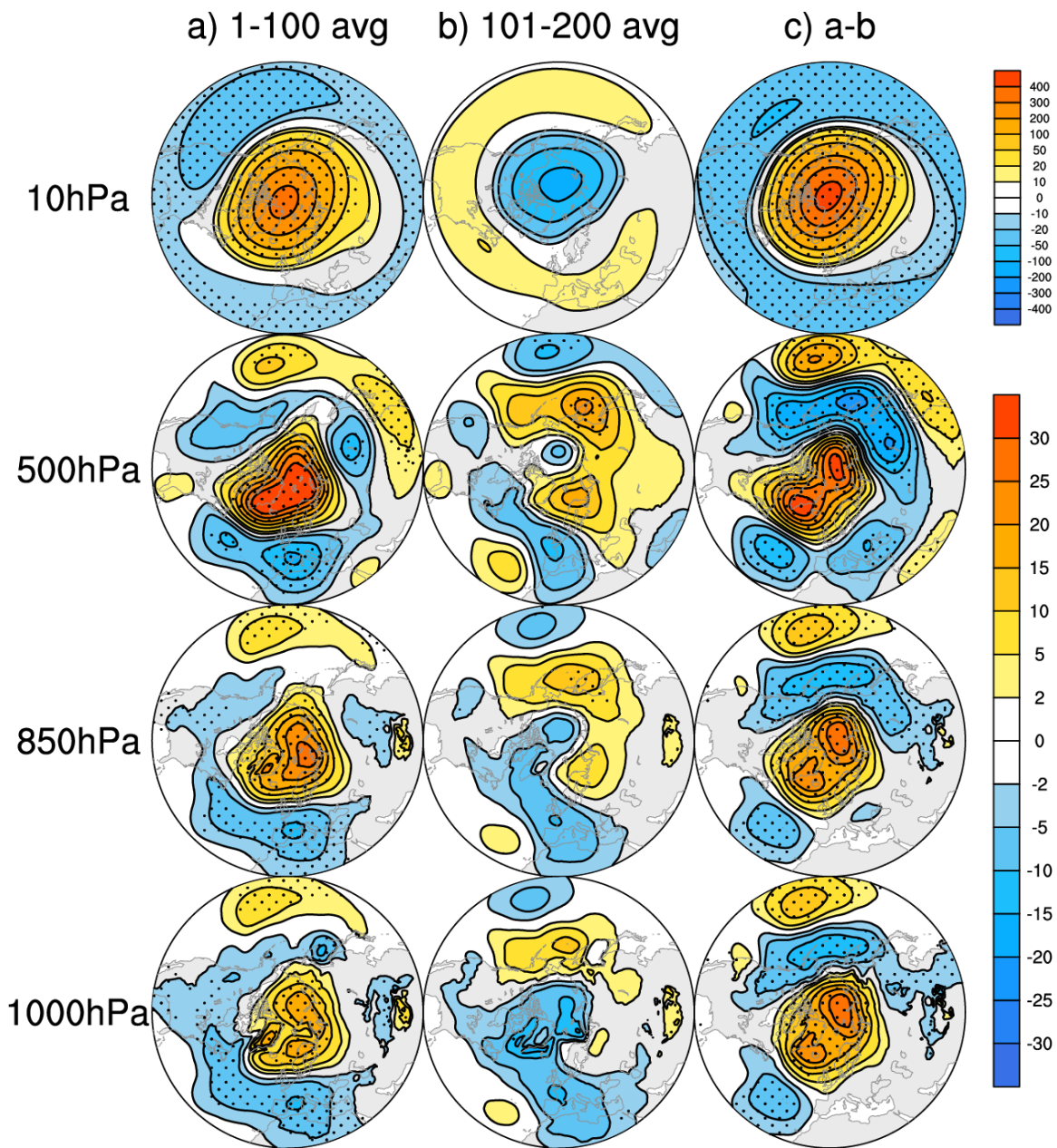
982

983 **Figure 4.** DJF zonal-mean zonal wind response (shading; m s^{-1}) as a function of pressure
 984 (hPa; y-axis) and latitude (x-axis) for $\Delta\text{past}_{\text{piSST}}$ based on: (a) all 200 members; (b)
 985 members 1-100; and (c) members 101-200. Black contours (interval of 10 m s^{-1} ; zero
 986 contour is thickened) indicate the climatology. Stippling indicates the 90% statistical
 987 significance based on a two-sided student's t-test and false discovery rate (FDR; Wilks
 988 2016).



990

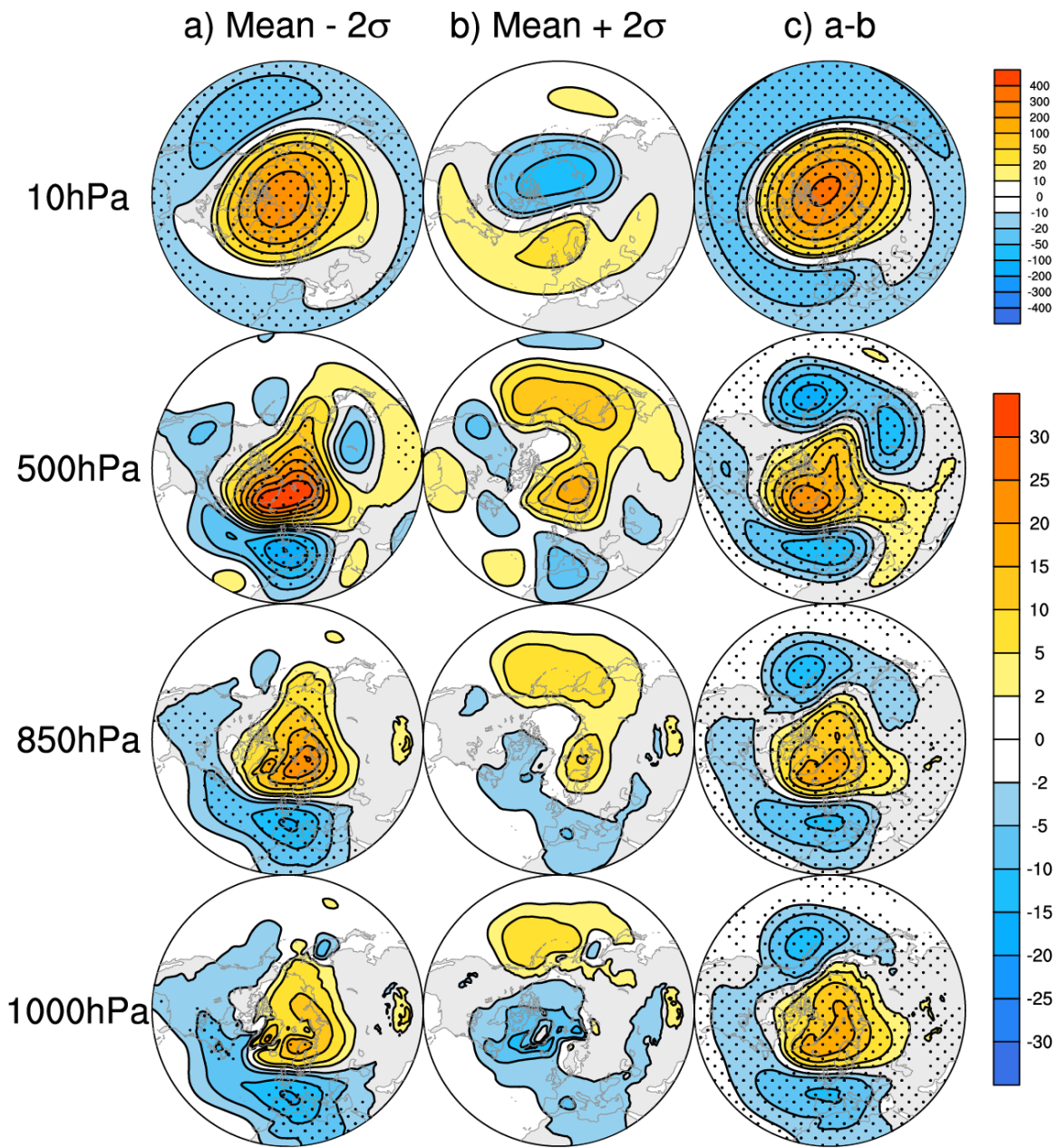
991 **Figure 5.** (Top) 60°N zonal-mean zonal wind response (m s^{-1}) in $\Delta\text{past}_{\text{piSST}}$ as a function
 992 of month (x-axis) and pressure (y-axis) for: (a) first 100-member average; (b) second 100-
 993 member average and (c) their difference. (Bottom) Regression analysis of 60°N zonal-
 994 mean zonal wind response onto U10 (defined as DJF zonal-mean zonal wind at 10 hPa and
 995 60°N) across the 1000 bootstrapped samples of 100-member averages. Panels d, e and f
 996 show the Mean- 2σ , Mean+ 2σ and their difference, respectively. Panel g shows the
 997 correlation of the zonal-mean zonal wind response with U10 across the 1000 bootstrapped
 998 samples. Stippling indicates the 90% statistical significance based on a two-sided student's
 999 t-test and false discovery rate.



1000

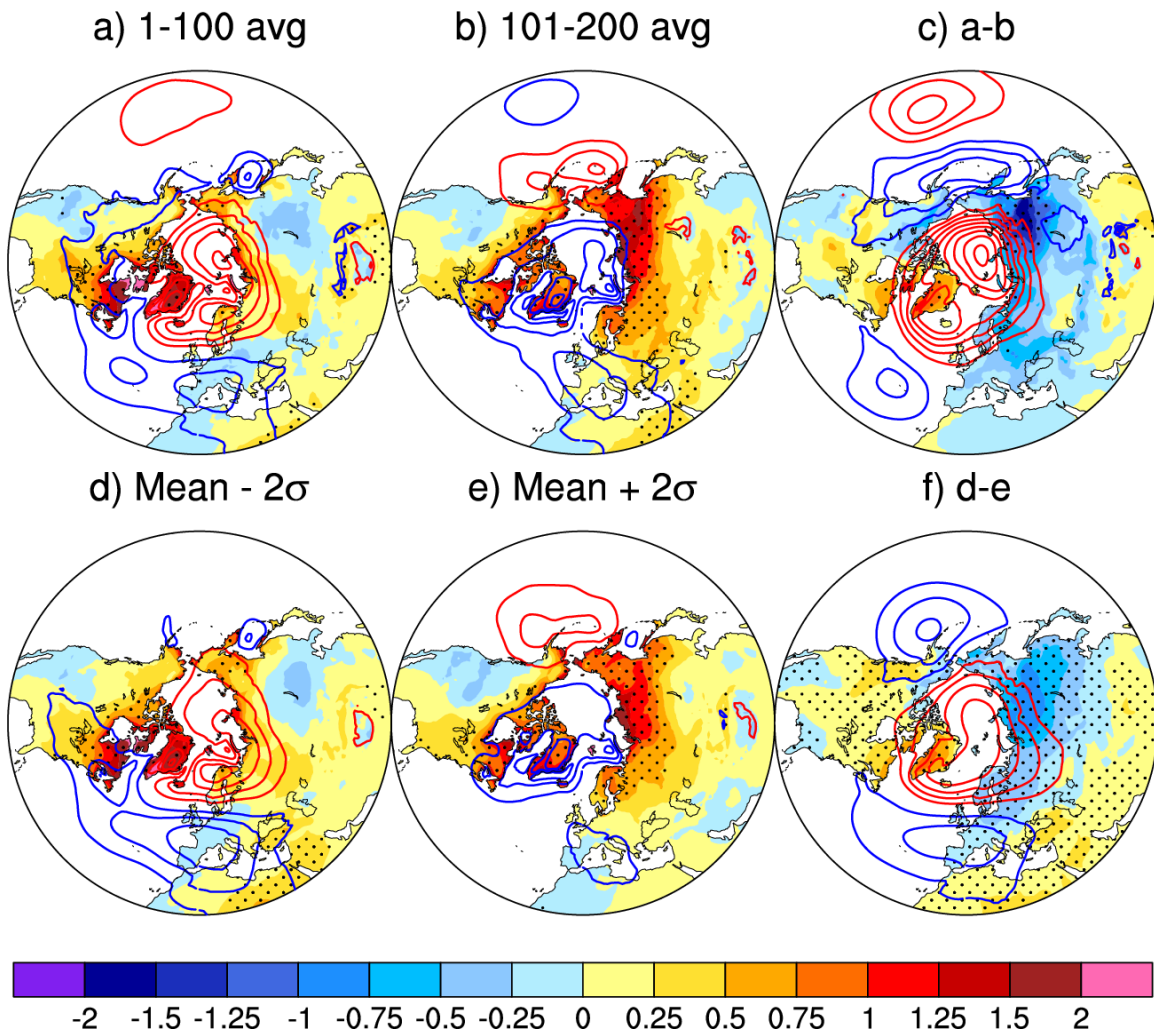
1001 **Figure 6.** Geopotential height response (m) in $\Delta_{\text{past}_{\text{piSST}}}$ for: (a) first 100-member average;
 1002 (b) second 100-member average and (c) their difference. Rows 1-4 show the 10-hPa DJF
 1003 response and the 500-hPa, 850-hPa and 1000-hPa responses in JFM, respectively. Stippling
 1004 indicates the 90% statistical significance based on a two-sided student's t-test and false
 1005 discovery rate.

1006



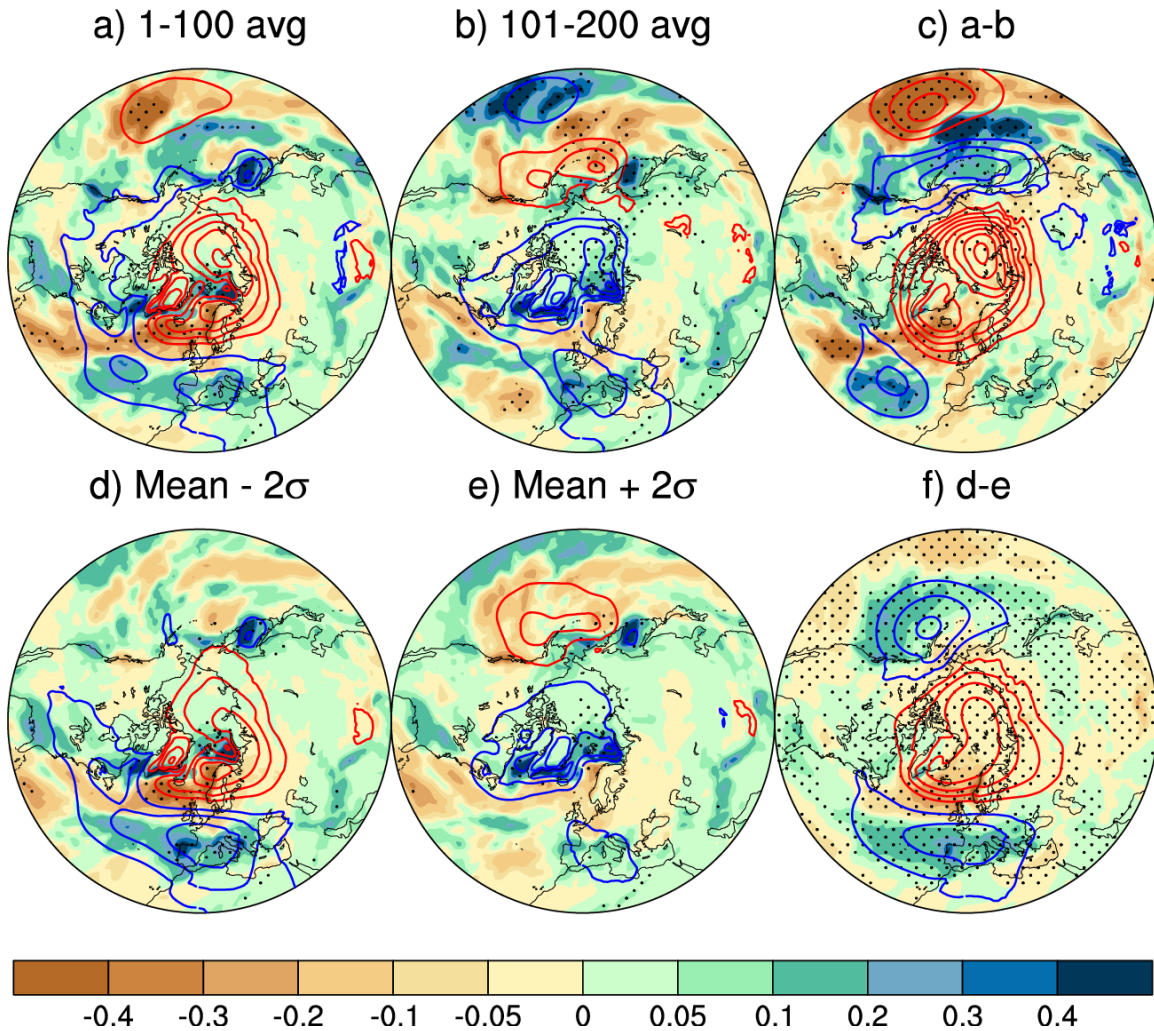
1007
 1008
 1009
 1010
 1011
 1012
 1013

Figure 7. Regression analysis of geopotential height response onto U10 in $\Delta\text{past}_{\text{piSST}}$ across the 1000 bootstrapped samples. Panels a, b and c show the Mean- 2σ , Mean+ 2σ and their difference, respectively. Rows 1-4 show the 10-hPa DJF response and the 500-hPa, 850-hPa and 1000-hPa responses in JFM, respectively. Stippling indicates the 90% statistical significance based on a two-sided student's t-test and false discovery rate.



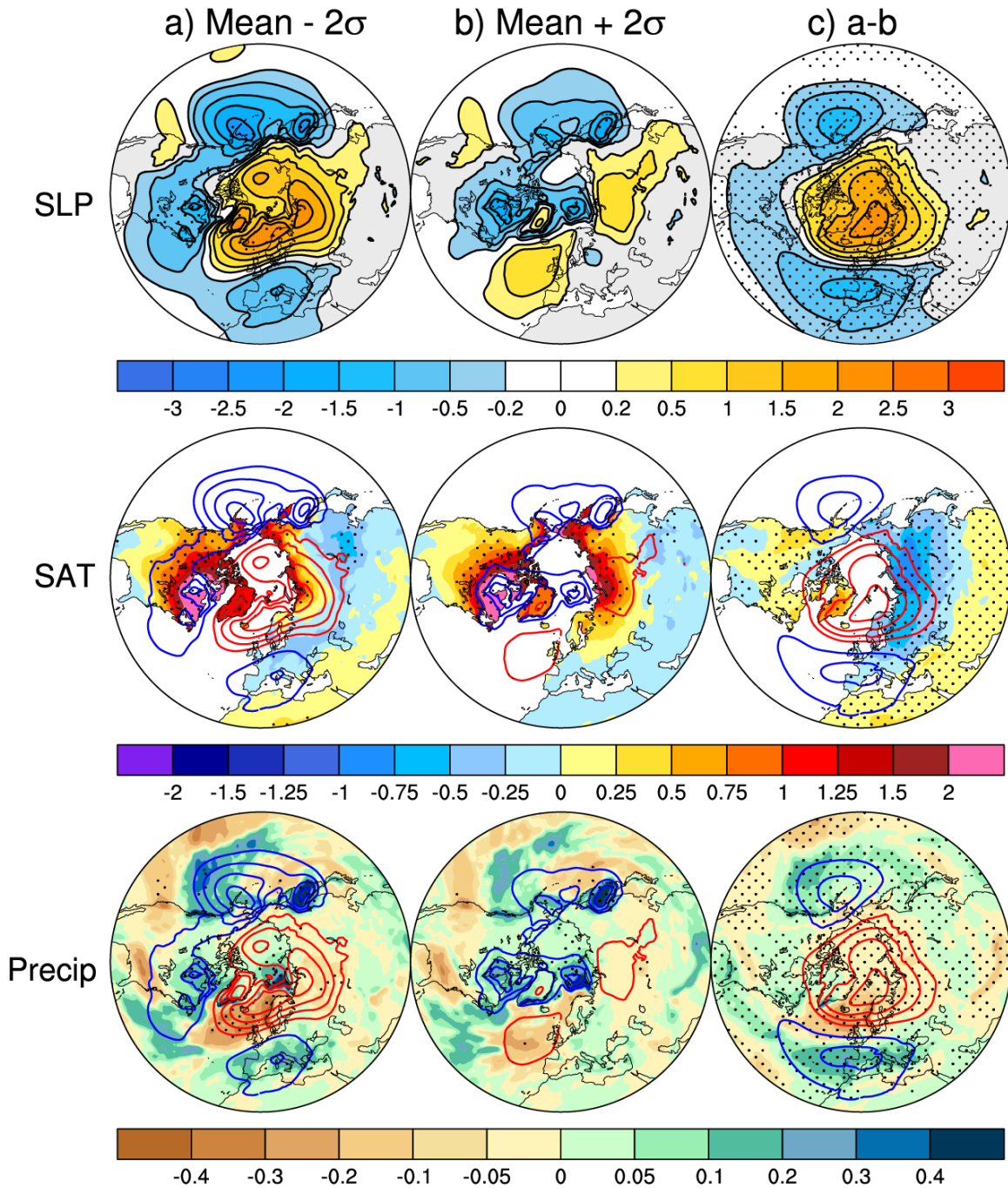
1014

1015 **Figure 8.** (Top) JFM SAT (shading; °C) and SLP (contours; interval of 0.5 hPa) responses
 1016 in $\Delta\text{past}_{\text{piSST}}$ for: (a) first 100-member average; (b) second 100-member average and (c)
 1017 their difference. (Bottom) regression analysis of JFM SAT response onto U10 in $\Delta\text{past}_{\text{piSST}}$
 1018 across the 1000 bootstrapped samples of 100-member averages. Panels d, e and f show the
 1019 Mean- 2σ , Mean+ 2σ and their difference, respectively. Red and blue contours denote
 1020 positive and negative values, respectively. Zero contour line has been omitted. Stippling
 1021 indicates the 90% statistical significance based on a two-sided student's t-test and false
 1022 discovery rate.



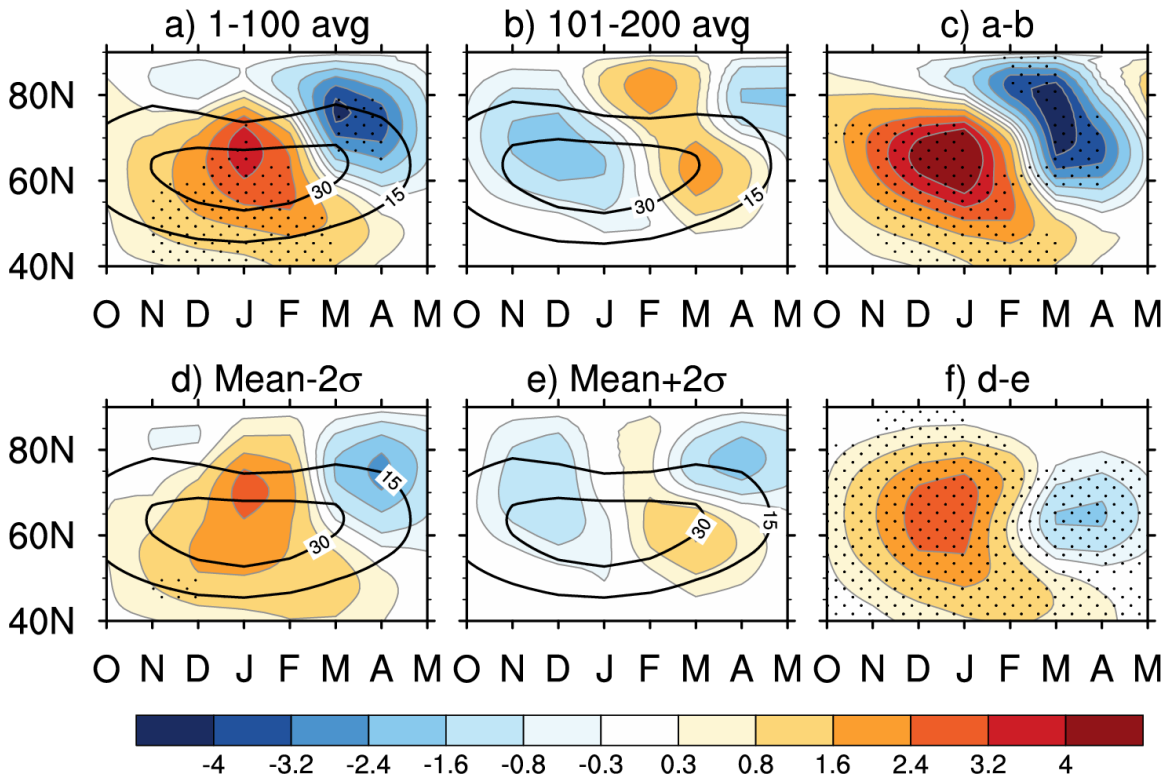
1023
 1024
 1025
 1026
 1027
 1028
 1029
 1030
 1031
 1032

Figure 9: (Top) JFM precipitation (shading; mm day⁻¹) and SLP (contours; interval of 0.5 hPa) responses in $\Delta\text{past}_{\text{piSST}}$ for: (a) first 100-member average; (b) second 100-member average and (c) their difference. (Bottom) regression analysis of JFM precipitation response onto U10 in $\Delta\text{past}_{\text{piSST}}$ across the 1000 bootstrapped samples of 100-member averages. Panels d, e and f show the Mean- 2σ , Mean+ 2σ and their difference, respectively. Red and blue contours denote positive and negative values, respectively. Zero contour line has been omitted. Stippling indicates the 90% statistical significance based on a two-sided student's t-test and false discovery rate.



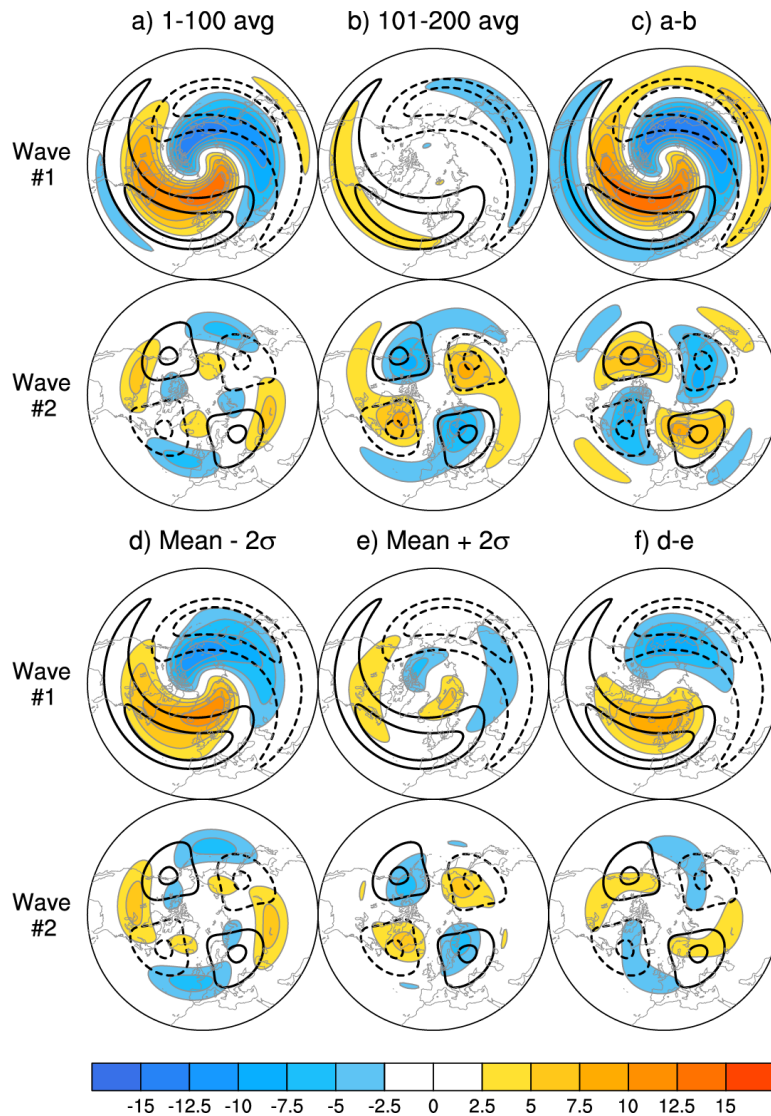
1033
 1034
 1035
 1036
 1037
 1038
 1039
 1040
 1041
 1042

Figure 10. Regression analysis of JFM response onto U10 in $\Delta\text{fut}_{\text{pdsst}}$ across the 1000 bootstrapped samples of 100-member averages. Rows 1-3 show the SLP (shading; hPa), SAT (shading; °C) and precipitation (shading; mm day⁻¹) responses, respectively. Panels a, b and c show the Mean- 2σ , Mean+ 2σ and their difference, respectively. The SLP responses (contours; interval of 0.5 hPa) are overlaid on the SAT and precipitation panels. Red and blue contours denote positive and negative values, respectively. Zero contour line has been omitted. Stippling indicates the 90% statistical significance based on a two-sided student's t-test and false discovery rate.



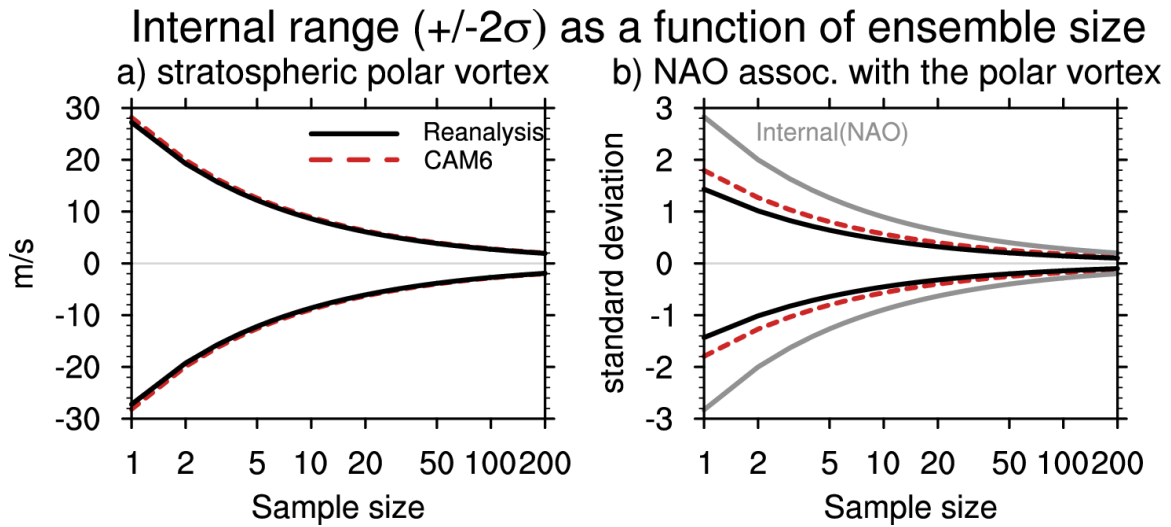
1043

1044 **Figure 11.** (Top) eddy heat flux response near 100 hPa (model hybrid 0.1 sigma level;
 1045 shading; K m s^{-1}) in $\Delta\text{past}_{\text{piSST}}$ as a function of month (x-axis) and latitude (y-axis) for: (a)
 1046 first 100-member average; (b) second 100-member average and (c) their difference.
 1047 (Bottom) Regression analysis of eddy heat flux response near 100 hPa onto U10 across the
 1048 1000 bootstrapped samples of 100-member averages. Panels d, e and f show the Mean- 2σ ,
 1049 Mean+ 2σ and their difference, respectively. Stippling indicates the 90% statistical
 1050 significance based on a two-sided student's t-test and false discovery rate. The
 1051 climatologies (contours; interval of 15 K m s^{-1}) are overlaid on the panels a, b, d and e.



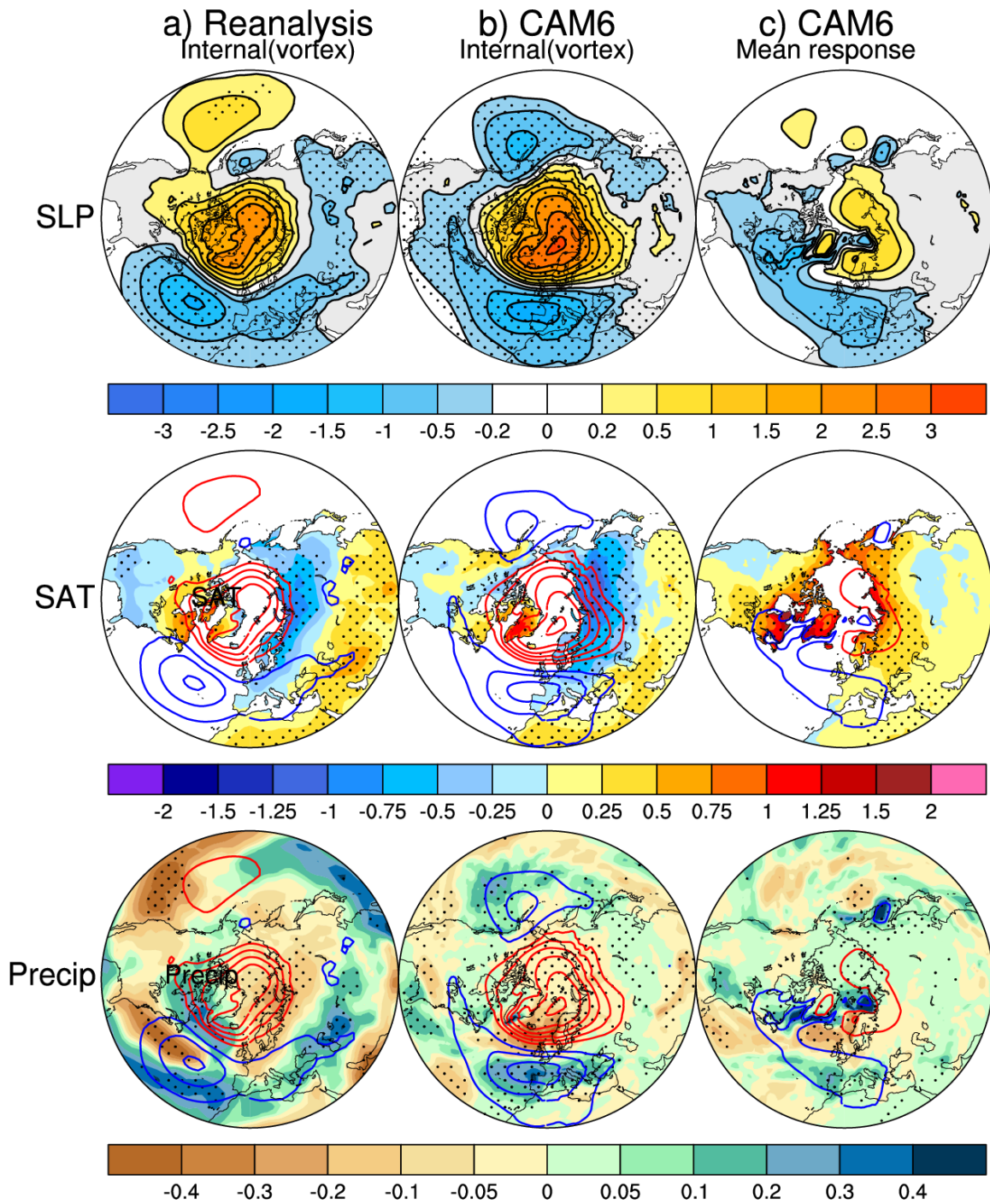
1052

1053 **Figure 12.** (Top two rows) NDJ zonal wave-1 and wave-2 responses (shading; m) at 300
 1054 hPa in $\Delta\text{past}_{\text{piSST}}$ for: (a) first 100-member average; (b) second 100-member average and
 1055 (c) their difference. The climatologies (contours; interval of 50 m) are overlaid on panels
 1056 a, b and c. (Bottom two rows) Regression analysis of NDJ zonal wave-1 and wave-2
 1057 responses at 300 hPa onto U10 in $\Delta\text{past}_{\text{piSST}}$ across the 1000 bootstrapped samples of 100-
 1058 member averages. Panels d, e and f show the Mean- 2σ , Mean+ 2σ and their difference,
 1059 respectively. The climatologies (contours; interval of 50 m) are overlaid on the panels d, e
 1060 and f. Solid and dashed contours denote positive and negative values, respectively. Zero
 1061 contour line has been omitted.



1062

1063 **Figure 13.** (a) 2.5th-to-97.5th percentile (2σ) range of variability in DJF U10 (m s^{-1}) as a
 1064 function of the number of ensemble members averaged (“sample size”) in Reanalysis data
 1065 (red curve) and CAM6 (black curve). (b) As in (a), but for the JFM NAO response
 1066 associated with \pm two standard deviation anomaly of DJF U10. Gray curve indicates the
 1067 total NAO internal variability ($\pm 2\sigma$) in Reanalysis and CAM6 (identical because each
 1068 NAO time series is standardized by its interannual standard deviation).



1069

1070 **Figure 14.** (a) 95% marginal error (2σ) of the JFM linear trend during the past 50 years
 1071 (1971-2020) for (from top to bottom): SLP (shading; hPa), SAT (shading; °C) and
 1072 precipitation (shading; mm day⁻¹) based on (a) NCEP-NCAR Reanalysis and (b) CAM6
 1073 (see text for details). The SLP trends are overlaid as contours (interval of 0.5 hPa) on the
 1074 SAT and precipitation panels. (c) The estimated forced response to Arctic sea ice loss over
 1075 the past 50 years from the CAM6 experiments (see text for details). Stippling indicates the
 1076 90% statistical significance based on a two-sided student's t-test and false discovery rate.